



Synthesis and characterization of titanium-substituted nanocrystalline Co₂-Y hexaferrite: magnetically retrievable photocatalyst for treatment of methyl orange contaminated wastewater

Mukesh Suthar¹ · Arup Kumar De² · Arindam Indra² · Indrajit Sinha² · Pradip Kumar Roy¹

Received: 20 October 2022 / Accepted: 16 January 2023 / Published online: 24 January 2023
© The Author(s), under exclusive licence to Springer-Verlag GmbH Germany, part of Springer Nature 2023

Abstract

Rapid industrial growth causes considerable environmental havoc, adversely affecting human and aqueous life. It becomes a significant concern to deal with adequate wastewater treatment strategies by converging on water scarcity. This research work explored the synthesis of titanium-substituted Y-type barium hexaferrite (Co₂-Y), having a general formula of Ba₂Co₂Fe_{12-x}Ti_xO₂₂ (x = 0.0, 0.1, 0.2, 0.3, 0.4, and 0.5), using a facile nitrate-based sol–gel auto-combustion route and its suitability was investigated as a heterogeneous catalyst within the photo-Fenton-based degradation of methyl orange (MO), one of the significant pollutants generated from textile industries. Developing a thermochemically stable and magnetically separable heterogeneous catalyst for photocatalytic decomposition of nonbiodegradable organic dye from wastewater was also emphasized. The as-prepared nanocrystalline Co₂-Y powders were analyzed using XRD, FTIR, DLS, UV–visible spectroscopy, SEM, VSM, and XPS. Furthermore, the photocatalytic degradation performance of pristine and titanium substituted

Responsible Editor: Guilherme L. Dotto

Highlights

- An attempt to use Ba₂Co₂Fe_{12-x}Ti_xO₂₂ ferrite for photocatalytic degradation of MO.
- Visualize the role of Ti⁴⁺ over the bandgap energy for catalytic activity.
- Ba₂Co₂Fe_{11.6}Ti_{0.4}O₂₂ exhibits its excellency in the presence of H₂O₂/visible light.
- Complete degradation of MO from wastewater (WW) occurs within 90 min.
- The boosted catalytic activity is elucidated with surface chemistry.
- A plausible pathway for MO degradation correlates with the creation of active OH[•].
- Catalyst is magnetically separable and reusable.
- Promising large-scale WW treatment without a hazardous footprint on the environment.

Novelty

• The photocatalytic degradation efficiencies of nanocrystalline Ba₂Co₂Fe_{12-x}Ti_xO₂₂ (x = 0.0, 0.1, 0.2, 0.3, 0.4, and 0.5) hexaferrites are evaluated to decompose methyl orange from wastewater in presence of H₂O₂/visible light. The results suggest that the Ba₂Co₂Fe_{11.6}Ti_{0.4}O₂₂ hexaferrite may offer its candidacy (improved thermochemical stability and enhanced apparent rate constant value) as a replacement of spinel ferrites to catalyze the degradation of several nonbiodegradable organic compounds from wastewater in large-scale industries without any hazardous footprint on the environment.

Ba₂Co₂Fe_{11.6}Ti_{0.4}O₂₂ ferrite, having the lowest bandgap value among all samples, was quantified and compared in terms of apparent rate constant (k_{arc}) value and turnover frequency values. The enriched photocatalytic performance was correlated with the existence of multi-valance states of transition metal cations and the availability of oxygen vacancy, confirmed by the surface chemistry using the XPS analysis. The modified (enhanced thermal and chemical stability) hexaferrite catalyst was magnetically separable and reusable without significant losses to its catalytic performance. This promising catalyst may be considered as a replacement for soft ferrite materials to catalyze the degradation of several other nonbiodegradable organic pollutants from wastewater in large-scale industries.

Keywords Y-type barium hexaferrite · Nanocrystalline · Wastewater treatment · Photocatalysis · Methyl orange · Hydrogen peroxide

Introduction

Water quality becomes an essential question in the present scenario due to the increasing rate of pollution. Although plenty of water is available over the earth's surface, only a fraction (around 0.03% of total water bodies) is convenient

Extended author information available on the last page of the article

for human activities. Water, a vital part of living beings, is deteriorating day by day with rapid industrial growth (Shah et al. 2022). This rapid industrial growth allows the discharge of various pollutants into the water bodies, adversely affecting water quality. Most of these industries, primarily concerned with paper, textile, leather, pharmaceuticals, food, packaging, and cosmetics, consume a huge number of dyes annually. A wide variety of chemicals are being utilized in industrial processing, starting from inorganic compounds to harsh organic and complex polymers. The textile industries occupy the largest share (around 60%) of the total consumption of organic dyes and harmful chemicals during the aqueous processing of clothes (Hai et al. 2007). Figure 1 shows that the water exposed to the untreated discharge of industrial waste contains several toxic, mutagenic, carcinogenic, and threatening compounds that cause esthetical pollution and perturbations to the aquatic (for both microbiological and fishes) along with human life (Hai et al. 2007; Shah et al. 2022).

The dyes are composed of skeleton, chromophore (groups having unsaturated or multiple bonding), auxochrome (enhances the color density), and soluble parts (helps to dissolve within solvent) (Auld 1907). These dyes can be categorized over different applications as direct dyes, vat dyes, acidic dyes, basic dyes, azo dyes, pigment-based dyes, natural dyes, and dispersed dyes (Benkhaya et al. 2017). Among all these dyes, only half (45 to 47%) of these dyes are found to be biodegradable. The remaining (53 to 55%) portion of these dyes is toxic to the ecosystem

and has become an issue of concern these days (Muhd Julkapli et al. 2014). Due to above mentioned adverse impact on the ecological system and human life, it has become crucial to develop a facile methodology to degrade these water-polluting agents, i.e., nonbiodegradable dyes.

There are several dyes and organic contaminants (studied for photocatalytic removal from wastewater), such as methylene red, methylene orange, congo red, tetracycline, oxytetracycline, chlortetracycline, Acid Blue 92, Acid Fuchsin, Acid orange 7, Acid Red B, Acid Red 138, Alizarine yellow, Brilliant blue-R, Congo red, Crystal violet, Direct Red 80, Direct Green 6, Erichrome black-T, Fuchsin Red, Indigo carmine, Methylene Blue, Methyl green, Methyl violet, Rhodamine B, Reactive blue 5, Titan yellow (Kefeni et al. 2017; Reddy and Yun 2016; Chen et al. 2020, 2022a, b), which adversely affect the water quality.

Methyl orange (MO) or orange III (dark red crystalline, odorless powder) (deep color, complex pollutant composition, high variation in water quality, high BOD and COD contents, poor biodegradability, highly toxic, carcinogenic, teratogenic, mutagenic, harmful to the environment and organisms) is an anionic azo-based organic nonbiodegradable dye, having a general molecular formula of $C_{14}H_{14}N_3NaO_3S$ [Molecular weight – 327.34 g. mol^{-1} , density – 1.28 g/cm^3 , melting point > 300 °C (573 K), solubility in water – 0.5 g/100 mL (20 °C)]. The structure of MO consists of a chromophore, auxochrome, and water-soluble group, as shown in Fig. 2 (PubChem CID 68,617; Mittal et al. 2007; Youssef et al. 2016; Yang

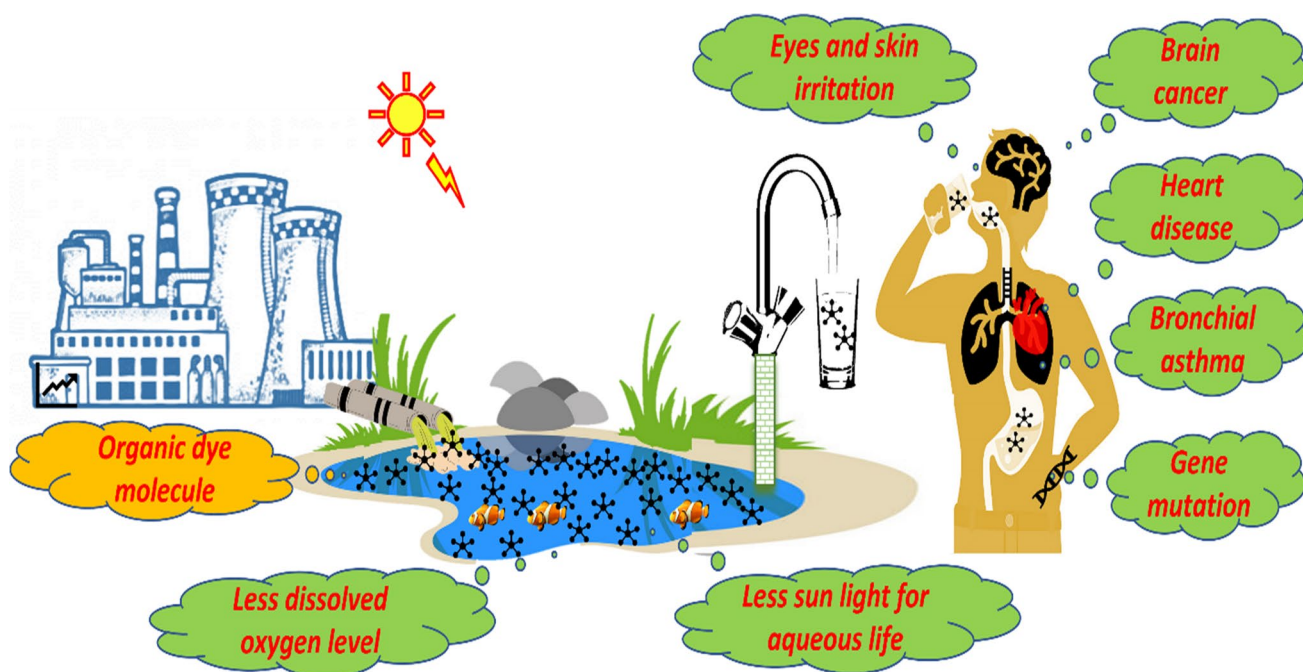


Fig. 1 Impact of nonbiodegradable dye-contaminated wastewater on human life and aquatic environment

et al. 2017; Aroke et al. 2020). It is widely utilized in the textile and printing industries. Approximately 10 to 15% of the initial concentration is disposed of directly into the water bodies or open environment while performing industrial processes (Aroke et al. 2020). The increasing utilization of MO in textiles, along with analytical industries and untreated disposal of this industrial waste within water bodies, have become a primary concern for the researchers.

To date, several strategies, i.e., Fenton-based reaction, flocculation, photocatalysis, precipitation, treating with hydrogen peroxide, adsorption on activated carbon or reduced graphene oxide sheets, treating with intense ultrasonic waves, air drag or inverse osmosis, oxidation using ozone, degradation using UV light irradiation within an aqueous solution, electrochemical degradation and electron beam irradiation, have been explored by the researchers to degrade these nonbiodegradable organic dyes (Meidanchi and Akhavan 2014; Valero-Luna et al. 2016; Shah et al. 2022). However, these processes may vary in expenditure, degradation effectiveness, and environmental issues. Among these, photo-Fenton-based degradation has been recognized as an outstanding technique due to its reasonably mild conditions, facile processing, and almost complete degradation of water-soluble organic dyes from water (Valero-Luna et al. 2016).

Traditionally, the homogenous Fenton technology has several drawbacks, i.e., a narrow range of acceptable pH levels, expensive precursors, and producing a considerable amount of iron sludge at the end of the process. To overcome these flaws, heterogeneously catalyzed Fenton technology is developed. To date, heterogeneously catalyzed Fenton technology (inexpensive, utilization of semiconducting soft ferrite materials, a broad range acceptance for pH level) has become the most effective and largely adaptable advanced catalytic oxidation process for treating industrial wastewater. Furthermore, the degradation rate is accelerated by UV–Vis light irradiation (Fallmann et al. 1999; Wang et al. 2014; Valero-Luna et al. 2016). The process involves the generation of exceedingly reactive hydroxyl radicals (OH^\bullet) by the catalytic dissociation of hydrogen peroxide (H_2O_2) within the presence of iron. The as-generated hydroxyl radicals (OH^\bullet) have a higher oxidation potential of 2.80 V and can easily oxidize or mineralize most of the organic molecules to produce H_2O , CO_2 , and other small molecules. It attacks most nonbiodegradable organic compounds (mainly unsaturated compounds) with zero selectivity (Liu et al. 2011; Valero-Luna et al. 2016; Singh et al. 2021).

Many researchers are also focused on photo-Fenton-based degradation of complex organic compounds, using iron-containing material systems (as a heterogeneous

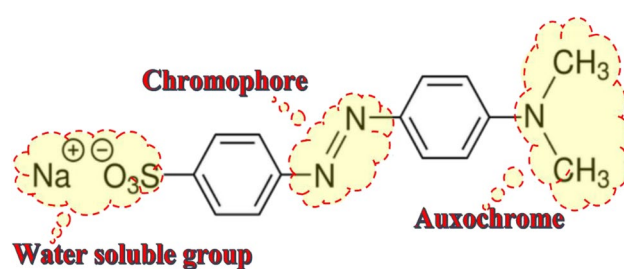


Fig. 2 Chemical structure of methyl orange (MO) dye

catalyst) having excellent redox configuration and moderate magnetic properties to facilitate the separation after completion of the reaction. To date, several iron oxide-based materials such as TiO_2 -coated Fe_2O_3 nanograin (Akhavan and Azimirad 2009), Polymer-coated Fe_2O_3 (Zhang et al. 2020a, b), and spinel ferrite-based catalysts such as CuFe_2O_4 , CoFe_2O_4 , FeFe_2O_4 (Wang et al. 2014), sulfur-modified ZnFe_2O_4 (Liu et al. 2011), MnFe_2O_4 with activated carbon (Nguyen et al. 2011), BaFe_2O_4 (Borse et al. 2011), NiFe_2O_4 (Sharma et al. 2015), MgFeCrO_4 (Moradnia et al. 2020), and CaFe_2O_4 (Dom et al. 2011) have been evaluated their suitability as a heterogeneous catalyst to decompose nonbiodegradable dyes from wastewater bodies. The poor thermochemical stability of these spinel ferrites restricts the utilization of these catalysts in a wide-scale application (Suthar et al. 2020). Researchers have investigated a few hard ferrite magnetic materials to overcome these stability issues due to their excellent thermochemical stability. The M-type strontium hexaferrite ($\text{SrFe}_{12}\text{O}_{19}$) is utilized to degrade the toluidine blue dye with a poor degradation rate ($3 \times 10^{-3} \text{ min}^{-1}$) (Farghali et al. 2008). For instance, M-type barium hexaferrite ($\text{BaFe}_{12}\text{O}_{19}$) also results in poor degradation (70.8%) of methylene blue (Valero-Luna et al. 2016). So, the interest of the researchers is restricted to the development of hard ferrite materials with enhanced degradation rate, total degradation of organic dyes, facile synthesis, higher diffusion capability, easy separation, and prolonged reusability. The facile extraction of the hard ferrite materials allows it to be categorized as an eco-friendly catalyst within the green chemistry approaches (Sharma et al. 2015; Valero-Luna et al. 2016).

In continuation to developing a stable and robust catalyst for the degradation of these organic wastes from water bodies, the Y-type barium hexaferrite ($\text{Co}_2\text{-Y}$) may be considered a suitable candidate due to their similar magnetic characteristics and redox configuration. It belongs to a hexagonal ferrite with several advantages over the spinel ferrites, such as better thermo-chemical stability, high Curie temperature (T_c), outstanding mechanical hardness, and corrosion resistance.

The Y-type barium hexaferrite ($\text{Co}_2\text{-Y}$) possesses a bandgap energy (around 0.74 to 2.35 eV) (Alrebdi et al. 2022), which is quite lower than the widely used photocatalyst anatase TiO_2 ($E_g = 3.2$ eV) (Yan et al. 2013) and other spinel ferrites such as CoFe_2O_4 (2.7 eV) (Holinsworth et al. 2013) and NiFe_2O_4 (2.5 eV) (Dolia et al. 2006). The capability to absorb the solar spectrum is determined by the bandgap (E_g) value of the ferrite being utilized as a photocatalyst. A narrow energy gap between the valence and conduction band provides a wider absorption of the solar spectrum; hence it can utilize visible light more efficiently (Yan et al. 2013). It is also suggested that the bandgap value can be minimized further by introducing titanium to the ferrite system. The incorporation of titanium generates impurity (especially donor-type) energy levels, which causes a narrow bandgap value within the system (Kumar and Kar 2014; Rajivgandhi et al. 2021).

In consideration of the leaching issue, the robust hexaferrite material (having enhanced thermochemical characteristics) may provide superior results. The experimental evidence performed by S. Jacobo et al. confirms the enhanced structural and chemical stability of barium hexaferrite material in comparison to the spinel type barium ferrite (barium monoferrite) (Jacobo et al. 2002). The environmental implications of the heavy metal ions such as barium, cobalt and iron can be prevented by treating the water further by utilizing several well established techniques such as carbon-based adsorbents (nanoporous adsorbents, especially activated carbons, carbon nanotubes, and graphene), chitosan-based adsorbents (a natural adsorptive polymer), mineral adsorbents (such as zeolite, silica, and clay), biosorbents, metal–organic framework based adsorbents, membrane-based filtration and separation, ultrafiltration (both micellar enhanced ultrafiltration and polymer enhanced ultrafiltration), reverse and forward osmosis, electrodialysis (to separate ions at the basis of electric potential difference), chemical-based separation (precipitation, flotation, coagulation and flocculation), electric-based separation (electrochemical reduction, electroflotation, and electrooxidation method), utilizing natural and synthetic allophane adsorbents (Al-Jlil 2010, 2017; El Sayed 2018; Kaveeshwar et al. 2018; Baldermann et al. 2018; Bilal et al. 2021; Chai et al. 2021; Qasem et al. 2021; Rathi and Kumar 2021).

Considering all the above factors, the present work describes the impact of titanium substitution on the structural, magnetic, and optical properties of the $\text{Co}_2\text{-Y}$ hexaferrite system. The sample having the least value of energy bandgap (E_g) is further characterized as a possible replacement of spinel ferrites for its catalytic degradation efficiency within photo-Fenton conditions (under visible light irradiation using a cool white LED and H_2O_2) utilizing methyl orange (MO) as a model dye molecule from the wastewater without any hazardous footprint on the environment.

Materials and methods

Materials

The reagents utilized for the synthesis of titanium-substituted Y-type barium hexaferrite ($\text{Co}_2\text{-Y}$) were barium nitrate [$\text{Ba}(\text{NO}_3)_2$], cobalt nitrate [$\text{Co}(\text{NO}_3)_3 \cdot 6\text{H}_2\text{O}$], iron nitrate [$\text{Fe}(\text{NO}_3)_3 \cdot 9\text{H}_2\text{O}$], titanium nitrate [$\text{Ti}(\text{NO}_3)_4 \cdot 4\text{H}_2\text{O}$], citric acid [$\text{C}_6\text{H}_8\text{O}_7 \cdot \text{H}_2\text{O}$], and ammonium hydroxide solution [NH_4OH]. The chemicals utilized for the dye degradation experiment were methyl orange [$\text{C}_{14}\text{H}_{14}\text{N}_3\text{NaO}_3\text{S}$], hydrogen peroxide [H_2O_2], and hydrochloric acid [HCl]. All chemicals were analytical grade and purchased from Sigma-Aldrich.

Synthesis of titanium substituted barium hexaferrite

Ultrafine nanocrystalline titanium-substituted barium hexaferrite having a general formula of $\text{Ba}_2\text{Co}_2\text{Fe}_{12-x}\text{Ti}_x\text{O}_{22}$ ($x = 0.0, 0.1, 0.2, 0.3, 0.4, \text{ and } 0.5$) were synthesized by nitrate-based auto combustion method using metal nitrates as precursors. Initially, the stoichiometric amounts of each precursor were calculated and dissolved within deionized (DI) water. The equimolar amount of citric acid (1:1:: metal nitrates: citric acid) was added to it and allowed to be homogenized using continuous magnetic stirring. Then the pH level was neutralized by the dropwise addition of ammonium hydroxide (30%) solution. The admixture was maintained at a temperature of 80 °C up to the transformation of the sol into a dried gel. The further heating of this dried gel resulted in the ignition, which allowed the formation of a fluffy powder (burnt ash). The as-obtained fluffy powders were pulverized and calcined at 1200 °C for a holding time of 2 h at a heating rate of 3 °C per minute. Finally, the sample was powdered using mortar-pestle and sieved using a 250-mesh sieve to be characterized as a catalyst. These powdered samples were pelletized with an addition of 3 wt.% polyvinyl alcohol (PVA) and sintered at 1100 °C for 2 h in an oxidizing atmosphere for thermomagnetic analysis.

Characterization of hexaferrite catalyst

The crystallite phase identification was performed by X-ray diffraction pattern (obtained from Rigaku MiniFlex 600 benchtop) using Cu-k_α radiation within the 2θ range of 20° to 80° and a step size of 0.02°. The presence of structural bonds was confirmed using FTIR spectra (obtained from Perkin Elmer BXIII FTIR infrared spectrometer), measured in transmittance mode within the range of 4000–400 cm^{-1} . The samples were dispersed within the isopropyl alcohol (IPA) to characterize their particle size distribution using a dynamic light scattering (DLS) based particle size analyzer (Zetasizer

Nano ZS by Malvern Panalytical). The optical properties (bandgap energy) of all the samples were analyzed using the UV- absorption spectrum (obtained from Shimadzu, UV 2600 UV–Vis spectrometer). The scanning electron micrographs, along with EDX spectra (obtained from ZEISS, EVO 18–2045), were used to examine the surface morphology and elemental purity of the sample. The room temperature hysteresis loop and thermo-magnetic behavior of the sintered pellets were measured using SQUID MPMS (Quantum design, Model-MPMS 3, EM-QM, USA) under an applied field of ± 6 T (60,000 Oe). Furthermore, the surface elemental identity and their chemical states were investigated using X-ray photoelectron spectra (K-alpha X-ray Photoelectron Spectrometer (XPS) by Thermo Scientific).

Photocatalytic degradation experiment

The photocatalytic degradation efficiency of the hexaferrite samples was evaluated by the degradation of methyl orange (MO). To examine the degradation efficiency, 0.1 mg of the dried hexaferrite sample was added to the 2 ml of aqueous MO solution (concentration 4.6 ppm) within a quartz cuvette (capacity of 4 ml) with a 1 cm of path length. The pH level of this suspension was tuned at three by the dropwise addition of 0.1 M HCl. The admixture was stirred continuously for the next 15 min (in the dark condition) to achieve the equilibrium condition for adsorption–desorption. Later, 100 μ l of 1.4 M hydrogen peroxide (H_2O_2) was introduced to it. Two protocols were implemented in the next step with two identical sets of the above-mentioned reaction mixture.

The aqueous solution of MO gives a unique UV–visible signature in the 200–800 nm range. Therefore, the decomposition of the dye was monitored with the dynamic UV analysis. The UV–Visible spectrum for the reaction mixture was allowed to be measured within an equal interval of 10 min for both Fenton (in dark conditions) and photo-Fenton (in the presence of a visible light source, a cool white LED emitting an irradiance of 720 $Watt/m^2$) in the wavelength range 400–800 nm). The intensities of all MO UV–visible peaks decreased with time, signifying the MO degradation. Moreover, MO degraded to small aliphatic entities because such molecules do not show any UV–visible signature.

Results and discussion

Structural analysis using XRD

The XRD pattern for the calcined powder of titanium substituted Co_2 -Y is shown in Fig. 3a. The presence of sharp characteristic peaks corresponding to the $Ba_2Co_2Fe_{12}O_{22}$ (standard JCPDS card no 44–0206) within the obtained

pattern confirms the formation of high purity Y-type barium hexaferrite (Co_2 -Y) phase along with good crystallinity. Furthermore, several structural parameters such as average crystallite size, lattice parameters, c/a ratio, unit cell volume, X-ray density, and lattice strain are obtained using the following equations, and the values are tabulated in Table 1 (Augustin and Balu 2017; Suthar et al. 2020).

$$D_{Avg.} = \frac{K_{sf} \cdot \lambda}{W_{hkl}^{act} \cdot \cos \theta} \quad (1)$$

$$W_{hkl}^{act} = \sqrt{(W_{hkl}^{meas.})^2 - (W_{hkl}^{instrumental})^2} \quad (2)$$

$$\frac{1}{d_{ip}^2} = \frac{1.34(h^2 + hk + k^2)}{a^2} + \left(\frac{l}{c}\right)^2 \quad (3)$$

$$V_{uc} = 0.8660 \cdot a^2 \cdot c \quad (4)$$

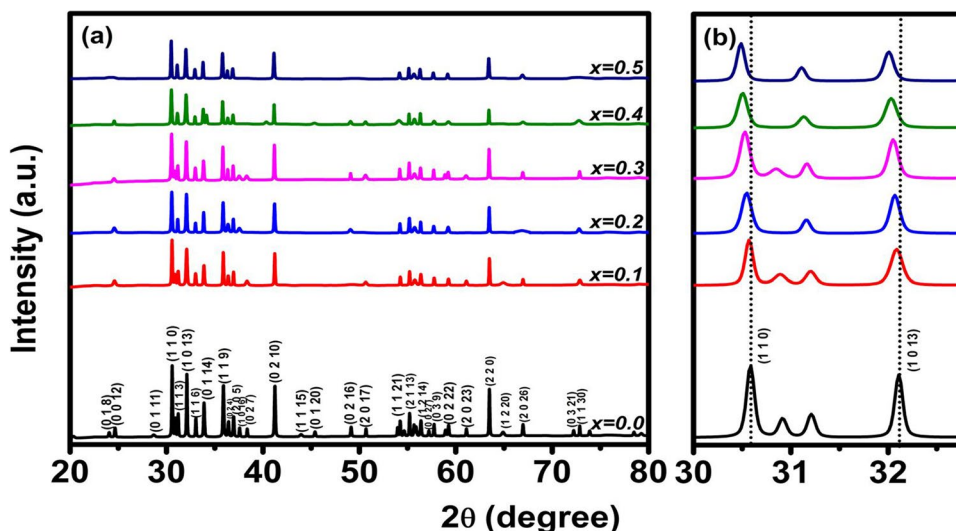
$$D_{x-ray} = \frac{M_w \cdot F}{N_a V_{uc}} \quad (5)$$

$$W_{hkl} \cdot \cos \theta = \epsilon_l \cdot (4 \cdot \sin \theta) + (\lambda k_{sf} / D_{Avg.}) \quad (6)$$

where $D_{Avg.}$ is the average crystallite size, K_{sf} signifies the Scherrer's constant ($K_{sf}=0.89$), λ is the wavelength of X-ray utilized for generating the XRD pattern ($\lambda=1.54056$ Å), W_{hkl}^{act} is the actual peak width at half of its maximum intensity (FWHM) in radians obtained by subtracting the instrumental contribution ($W_{hkl}^{instrumental}$) from the measured value ($W_{hkl}^{meas.}$) and θ is the peak position or Bragg's angle, d_{ip} is the inter-planer spacing (distance between two sequential atomic planes), h k and l are miller indices (group of numbers indicating the orientation of any particular atomic plane), a and c are the lattice parameters representing the minor and major axis of a hexagonal lattice, V_{uc} signifies the volume of a unit cell, D_{x-ray} signify the X-ray density. That is, crystal structure-dependent theoretical density, M_w represents the molecular weight, F is the number of effective formula units existing within a solo unit cell ($F=3$ for Co_2 -Y), N_a is Avogadro's constant having a numeric value of 6.023×10^{23} , and ϵ_l is lattice strain due to the crystal imperfections or lattice dislocations.

The XRD pattern confirms the successful substitution of Ti^{4+} at the Fe^{3+} site. It is found that the crystallite size is in the range of 64–72 nm and decreases with substitution. The XRD results agree with the substitution of a larger cation Ti^{4+} (0.68 Å), at the site of a smaller cation Fe^{3+} (0.64 Å) by increasing the value of the lattice parameters along with the unit cell volume (Jia et al. 2013). A peak shifting (Fig. 3b) is observed towards the left side. The crystal axis ratio (c/a) is found to be 7.429 for $x=0.0$ and

Fig. 3 XRD patterns of calcined Ba₂Co₂Fe_{12-x}Ti_xO₂₂ (x=0.0, 0.1, 0.2, 0.3, 0.4, and 0.5) ferrite powders



7.421 for $x=0.5$, which lies within the permissible range for the formation of the Co₂-Y phase (Suthar et al. 2020). The X-ray densities follow the decreasing trend with substitution. It is in good agreement with both the decreasing molecular weight and the increasing unit cell volume. The crystallite distortions that arise while substituting a larger cation at the smaller cation site are quantified using the determination of lattice strain using the Williamson-Hall method to Eq. (6), where the lattice strain (ϵ_l) is measured as the slope of the straight line obtained by linear fitting to the curve between $W_{hkl} \cdot \cos\theta$ and $4 \cdot \sin\theta$, as depicted in Fig. 4 (Augustin and Balu 2017). The lattice strain is found to be positive (volumetric expansion within the unit cell) for all these samples, which keeps rising continuously with increasing Ti⁴⁺ ions substitution.

FTIR analysis

The structural variations within the titanium-substituted Y-type barium hexaferrite (Co₂-Y) are analyzed further using FTIR spectra by confirming the presence of various characteristic bands corresponding to their specific absorption peak positions. In Fig. 5,

the FTIR spectra for undoped ($x=0.0$) calcined powder consists of two major absorption peaks, one at 400.15 cm⁻¹ (corresponding to asymmetric stretching of metal cation at the octahedral site) and the second at 584.32 cm⁻¹ (corresponding to asymmetric stretching of metal cation at the tetrahedral site). It is considered the characteristic peak for the cationic vibrations within the spinel block of the Co₂-Y structure (Adeola et al. 2016).

The substitution of Ti⁴⁺ ions at the Fe³⁺ site allows a slight shifting of these characteristic bands towards the higher wavenumber with increasing concentration. The structural variations can be quantified with the help of determining Fe–O bond lengths using the following equation:

$$B_l = \sqrt[3]{(17/F_c)} \tag{7}$$

$$F_c = (2\pi\nu_{wn}c_{vl})^2 \cdot \mu_a = (2\pi\nu_{wn}c_{vl})^2 \cdot [(A_{w1} x A_{w2}) / (A_{w1} + A_{w2})] \tag{8}$$

where B_l represents the bond length, F_c is for force constant (reflects the bond stiffness), ν_{wn} is the corresponding wavenumber for a specific absorption band, c_{vl} is the light velocity measured in a vacuum having

Table 1 Crystallite size, lattice constants (a and c), (c/a) ratio, unit cell volume, X-ray density, and lattice strain of the calcined Ba₂Co₂Fe_{12-x}Ti_xO₂₂ ($x=0.0, 0.1, 0.2, 0.3, 0.4, \text{ and } 0.5$) ferrite powders

Composition	Crystallite size (nm)	Lattice parameters		Axial ratio (c/a)	Unit cell volume (Å ³)	X-ray density (g/cm ³)	Lattice strain (ϵ)
		a (Å)	c (Å)				
$x=0.0$	72.27	5.844	43.417	7.429	1284.314	5.266	6.75×10^{-4}
$x=0.1$	69.07	5.845	43.411	7.426	1284.608	5.262	8.95×10^{-4}
$x=0.2$	67.17	5.852	43.459	7.426	1289.114	5.240	3.85×10^{-3}
$x=0.3$	64.19	5.853	43.463	7.426	1289.444	5.236	4.27×10^{-3}
$x=0.4$	64.09	5.861	43.511	7.424	1294.222	5.213	5.34×10^{-3}
$x=0.5$	64.01	5.864	43.515	7.421	1295.826	5.204	5.62×10^{-3}

a numerical value of 3×10^8 m/s, μ_a is the effective mass of constituting atoms, A_{w1} and A_{w2} are the atomic weights of linked atoms. The force constant (F_c) associated with the Fe–O bond and respective bond length (B_i) values are listed in Table 2. The results show that the Fe–O bond length is increased with the substitution of Ti^{4+} within the hexaferrite (Co_2Y). The bond length variation can be correlated due to the ionic radius mismatch (introducing a larger cation at a smaller cation site), which also favors the volumetric expansion suggested by XRD studies. Apart from these two characteristic peaks, the co-existence of a few minor absorption peaks in the range of 1064.03 to 1626.66 cm^{-1} is also observed. It may be attributed due to the presence of metal–oxygen–metal bonding, likewise Fe–O–Fe or Co–O–Co (between 1100 and 1500 cm^{-1}), or the presence of residual traces of N–O stretching vibration (between 1475 and 1550 cm^{-1}), or N–H band (between 1600 and 1640 cm^{-1}). It may also be associated with using an ammonia solution while adjusting the pH. The peaks around 1626 cm^{-1} and 3440 cm^{-1} may be ascribed to the O–H stretching vibrations due to the adsorbed moisture content at the surface (Lalegani and Nemati 2015; Adeela et al. 2016).

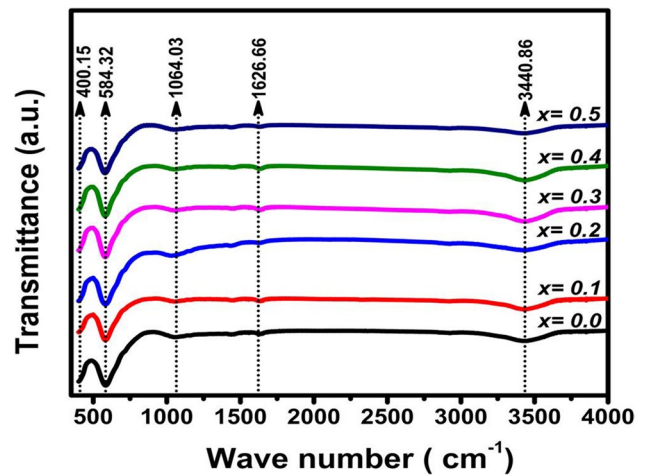
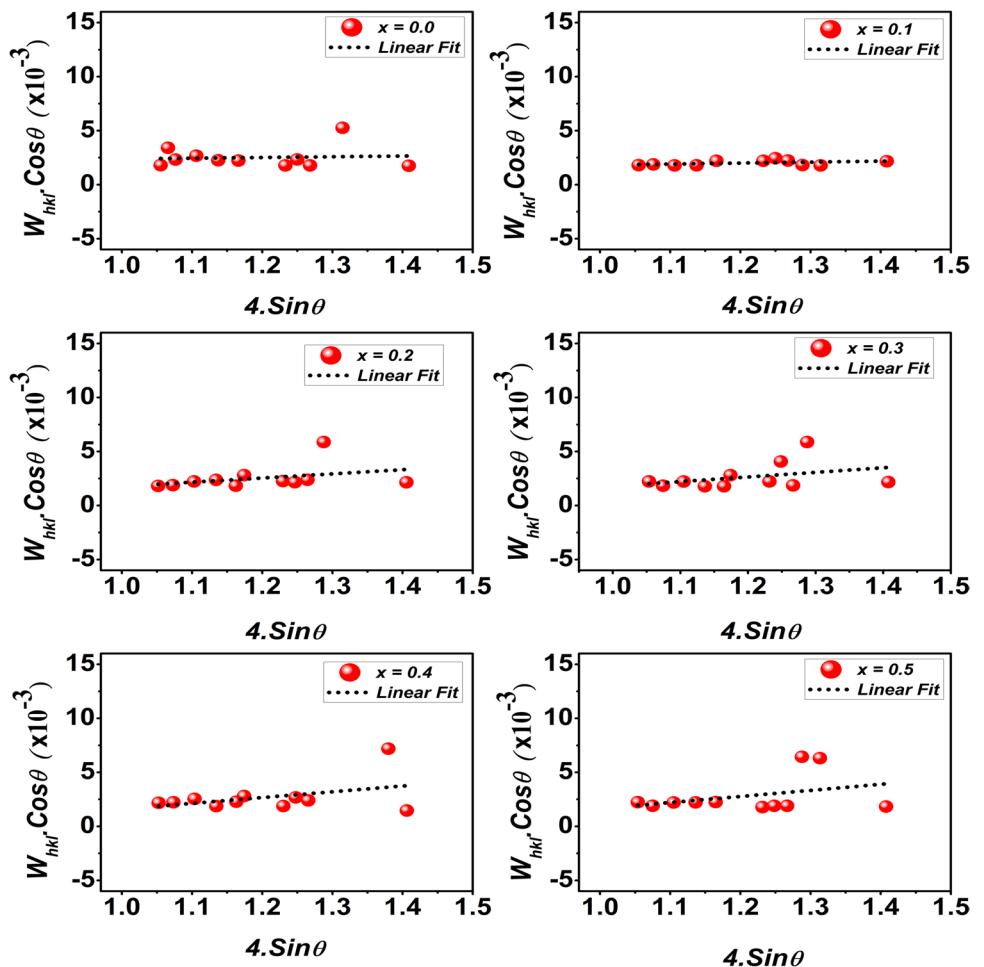


Fig. 5 FT-IR spectra of calcined $Ba_2Co_2Fe_{12-x}Ti_xO_{22}$ ($x=0.0, 0.1, 0.2, 0.3, 0.4,$ and 0.5) ferrite powders

Fig. 4 Williamson–Hall plot for calcined $Ba_2Co_2Fe_{12-x}Ti_xO_{22}$ ($x=0.0, 0.1, 0.2, 0.3, 0.4,$ and 0.5) ferrite powders



Particle size distribution analysis

All the calcined hexaferrite samples dispersed within the isopropyl alcohol (IPA) are analyzed for their average particle size (APS) along with poly-dispersion index (PdI),

using the dynamic light scattering-based technique (as shown in Fig. 6). The results suggest that particle sizes are found to be in decreasing order (from 1.835 μm for $x = 0.0$ to 1.055 μm for $x = 0.5$) with Ti^{4+} substitution within the Co_2 -Y hexaferrite. The particle size distribution quality can be explained by Pdl value, which indicates the non-uniformity of the powder sample on a scale of 0 to 1 (Dan-aei et al. 2018). The results suggest that all these samples consist of a wide range of size distribution owing to their platelet-like shape and the substitution of Ti^{4+} leads to the lower Pdl value.

Magnetic property analysis

To investigate the influence of Ti^{4+} ions substitution on the magnetic properties of Y-type barium hexaferrite (Co_2 -Y), the magnetization curves are recorded at 300 K (as shown in Fig. 7) at a maximum applied field of ± 6 Tesla. The results suggest the ferrimagnetic behavior in all synthesized samples. The sample doesn't achieve saturation within the applied magnetic field range; the exact saturation magnetization value is estimated at the high-field regime using the Stoner–Wohlfarth law of approach. The law of approach describes the dependency of magnetization over the H^{-2} , where the magnetization value can be described using the following expression (Fattouh et al. 2021);

$$M = M_s [1 - I_p/H - M_a/H^2] + H \cdot \chi_\infty \tag{9}$$

where M_s signifies the exact value of saturation magnetization. I_p and M_a are inhomogeneity and magneto-crystalline anisotropy-dependent parameters, which describe the magnetic anisotropy and microstructural environment within the system. χ_∞ signify materials susceptibility at a high magnetic field (H). The value of the inhomogeneity constant (I_p) and additive term ($H \cdot \chi_\infty$), which represent the field-encouraged magnetization, may be ignored within the presence of a high magnetic field and underneath the Curie temperature (T_c) of that material. In consideration of both circumstances, the expression for magnetization can be rearranged as follows:

$$M = M_s [1 - M_a/H^2] \tag{10}$$

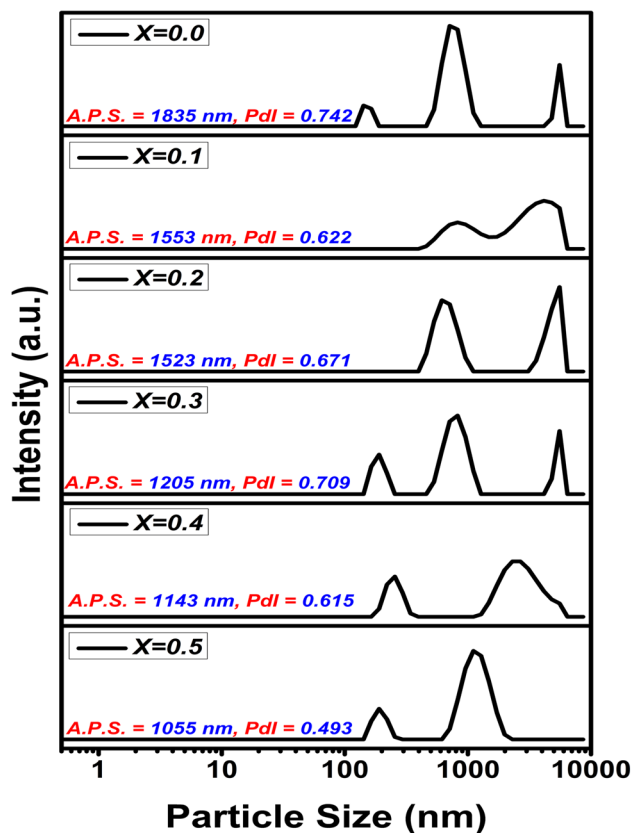


Fig. 6 DLS analysis for the particle size distribution of $Ba_2Co_2Fe_{12-x}Ti_xO_{22}$ ($x = 0.0, 0.1, 0.2, 0.3, 0.4, \text{ and } 0.5$) ferrite powders

The exact value for saturation magnetization can be obtained by considering the above-mentioned expression equivalent to a straight-line equation. By plotting the M vs. H^{-2} graph, the Y-axis intercept (using linear fitting to the data points, as shown in Fig. 8) provides the exact value of saturation magnetization (Lee et al. 2020; Fattouh et al. 2021). To govern the impact of the substitution over the magnetic properties of a ferrite system, the numbers of Bohr magneton (N_{bm}) and magnetic anisotropy constants (K_f) are also determined using the following relations (Almessiere et al. 2019; Tchouank Tekou Carol et al. 2020);

Table 2 Characteristic wave number, effective mass for Fe–O bond, force constant, and corresponding bond length of the calcined $Ba_2Co_2Fe_{12-x}Ti_xO_{22}$ ($x = 0.0, 0.1, 0.2, 0.3, 0.4, \text{ and } 0.5$) ferrite powders

Composition	Wave number (cm ⁻¹)	Effective mass (10 ⁻²⁶ kg)	Force constant (N/cm)	Bond length (Fe–O) (Å)
$x = 0.0$	584.3255	2.0648	2.5039	1.8935
$x = 0.1$	582.8792	2.0648	2.4915	1.8966
$x = 0.2$	582.3970	2.0648	2.4874	1.8977
$x = 0.3$	581.4328	2.0648	2.4792	1.8998
$x = 0.4$	580.9507	2.0648	2.4751	1.9008
$x = 0.5$	579.9865	2.0648	2.4669	1.9029

$$N_{bm} = \frac{M_w X M_s}{5585} \quad (11)$$

$$K_1 = \left(\frac{\mu_0}{2} \right) M_s \cdot H_c \quad (12)$$

where M_w is the molar weight of the hexaferrite sample, M_s is the saturation magnetization, H_c is the coercivity field, and μ_0 is the vacuum permeability having a numerical value of 12.57×10^{-7} H/m).

To evaluate the variation of temperature-dependent magnetization properties with Ti^{4+} ion substitution, thermomagnetic curves (ZFC and FC) are obtained within the temperature range of 300 to 900 K at an applied field of 300 Oe, as shown in Fig. 9. The Curie temperature (T_c) (Inserted Figures in Fig. 9) is measured at the minima from the temperature-dependent first-order derivative (dM/dT) curve. All the derived parameters such as saturation magnetization (M_s), coercivity field (H_c), remnant magnetization (M_r), number of Bohr magneton (N_{bm}), squareness ratio (M_r/M_s), magnetic anisotropy constant (K_1), and Curie temperature (T_c) are calculated and tabulated in Table 3.

The results suggest that the value of saturation magnetization (M_s) along with the number of Bohr magneton (N_{bm}) is found to be decreased with the substitution of titanium ions within the hexaferrite. This decreasing behavior can be explained by the replacement of a magnetic (Fe^{3+}) ion with a nonmagnetic (Ti^{4+}) ion within a hexaferrite system (Kumar et al. 2017). The coercivity values are found to be increased linearly up to the $x=0.2$ and achieved their maximum value of 222.24 Oe. The improvement of the coercive field may be due to the enhanced value of lattice imperfections with nonmagnetic inclusion within the system, generation

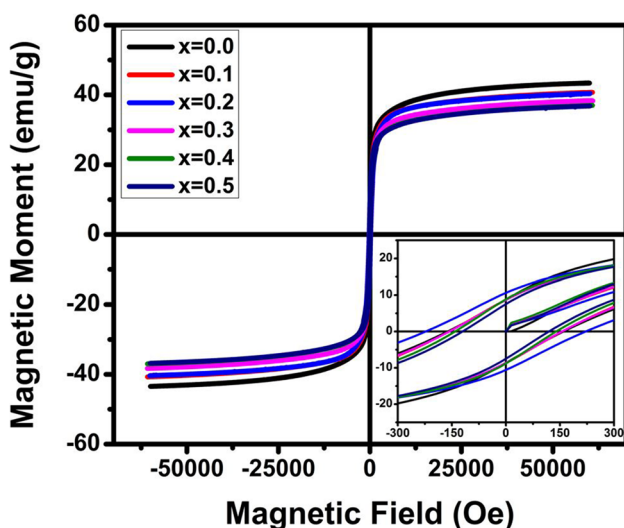


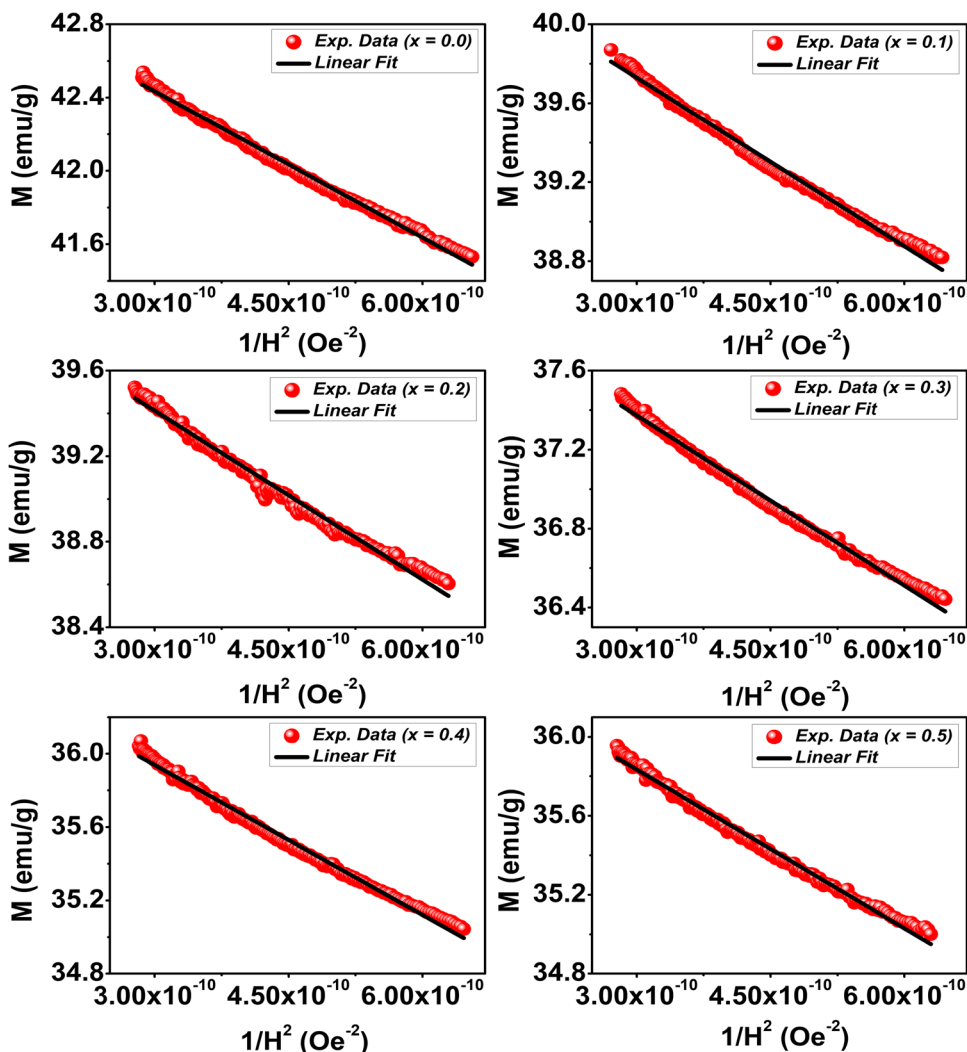
Fig. 7 Magnetic hysteresis loops of calcined $Ba_2Co_2Fe_{12-x}Ti_xO_{22}$ ($x=0.0, 0.1, 0.2, 0.3, 0.4, \text{ and } 0.5$) ferrite powders

of $Fe^{2+}-Ti^{4+}$ pair by replacement of two Fe^{3+} ions, having larger magneto-crystalline anisotropy, larger ionic radius, and enhanced lattice strain value (Ounnunkad 2006; Rao et al. 2009; Kumar et al. 2018). Further increment of Ti^{4+} content allows for a decrease of coercive field. It can be explained by lowering the anisotropy constant value or decreasing the average particle size value along with the dominance of single-domain particles (nearly $1.18 \mu m$) (Park et al. 2015; Hosseinkhan Nejad et al. 2017; Kumar et al. 2018).

The retentivity value (magnetization holding capability after removal of the externally applied field) shows a random behavior with substituting Ti^{4+} ions. This random behavior can be explained by the ferroxplana nature of Co_2-Y hexaferrite, where the preferred plane of magnetization is found to be within its basal plane or in a right circular cone at an angle to the major c -axis. Sometimes the magneto-crystalline anisotropy field may reorient this plane of magnetization without affecting the overall saturation magnetization and coercivity of that material (Pul-lar 2012; Zhang et al. 2014). The squareness ratio values (explain the anisotropy-dependent magnetic hardness of that system) are found to be within 0.2023 to 0.2622 and lie within the range of $0.05 < M_r/M_s < 0.50$. It implies that all these magnetic particles are of the pseudo-single domain in nature and coupled magneto-statically to each other (Adeela et al. 2016). The magnetic anisotropy values are found in good agreement with the coercivity (H_c). In consideration of the earlier reported studies, the substitution of Ti^{4+} ions with Fe^{3+} ions is expected to the overall decreasing behavior for magnetic anisotropy constant (K_1) (Kakol et al. 1994; Rao et al. 2009). The only abnormalities associated with the sample $x=0.2$ results may be due to the dependency of the magnetic anisotropy constant over the occupancy site and the discrete contribution of Fe^{2+} ions (Fletcher and O'Reilly 1974; Kakol et al. 1994).

The thermomagnetic analysis of all these hexaferrite samples confirms the existence of a sharp ferromagnetic (FM) to paramagnetic (PM) phase transition within it. This transition temperature is determined with the help of a temperature-dependent first-order derivative (dM/dT) curve of magnetization. The presence of an intense downward peak is measured for the transition temperatures of each sample. The Curie temperature for the undoped Co_2-Y sample is found to be 603.76 K, which is in good agreement with the earlier reported value of 600 K by S.G. Lee et al. (Lee and Kwon 1996). This transition temperature shows a reverse trend with increasing the substitution of Ti^{4+} within the system. It can be explained based on the exchange interactions. The exchange interaction within the ferrite system decreases both magnetic ion density and overall magnetic moment value; hence, lesser amount of thermal energy is required to surpass the weak exchange interaction of that sample. The substitution of diamagnetic Ti^{4+} replaces a magnetic ion Fe^{3+} ,

Fig. 8 M vs. H^{-2} plot (Stoner–Wohlfarth model) of calcined $\text{Ba}_2\text{Co}_2\text{Fe}_{12-x}\text{Ti}_x\text{O}_{22}$ ($x=0.0, 0.1, 0.2, 0.3, 0.4,$ and 0.5) ferrite powders



resulting in the lowering of exchange interactions within the system, and the Curie temperature shows a decreasing behavior (Rao et al. 2009).

UV–Visible spectrum analysis

A diffuse reflectance-based-UV–Visible spectrum is studied with all calcined powders to examine the optical characteristics (a crucial factor in designing photocatalysts). The as-obtained absorption spectra within a wavelength range of 200 to 1400 nm (as displayed in Fig. 10) clearly signify the enhanced absorption of photons for titanium-substituted samples as compared to the pure $\text{Co}_2\text{-Y}$ sample. The band-gap energy (E_g) is the distance between the valance band (highest occupied orbit) and conduction band (lowest unoccupied orbit). This energy gap (E_g) can be measured either in terms of direct bandgap (measured vertical energy distance) or indirect bandgap (measured obliquely or inclined energy distance). To determine the energy band gap value (E_g) for

all these hexaferrite samples, the Tauc relationship can be utilized as follows (Mohammed et al. 2021):

$$\frac{(\alpha \cdot h_p \cdot \nu)}{K_T} = (h_p \nu - E_g)^Q \quad (13)$$

Here, α is the coefficient of absorption, h_p represents the plank constant having a numerical value of 6.626×10^{-34} J.s, ν is the incident photon frequency, K_T is an energy-independent constant, and Q is dependent on the type of the transition such as $1/2$ and $3/2$ for allowed and forbidden direct transition, 2 and 3 for allowed and forbidden indirect transition (Naseri and Ghasemi 2016; Carol et al. 2020).

All these hexaferrite samples demonstrate energy bandgap (E_g) value corresponding to the allowed direct transition with $Q = 1/2$ using linear extrapolation to the graph between $(\alpha \cdot h_p \cdot \nu)^2$ and E_g ; the obtained values are mentioned within the inset of Fig. 10. The results suggest that the bandgap energy is found to be decreased linearly

Fig. 9 Magnetization along and its first order derivative (dM/dT) as a function of temperature (K) for calcined $Ba_2Co_2Fe_{12-x}Ti_xO_{22}$ ($x = 0.0, 0.1, 0.2, 0.3, 0.4,$ and 0.5) ferrite powders

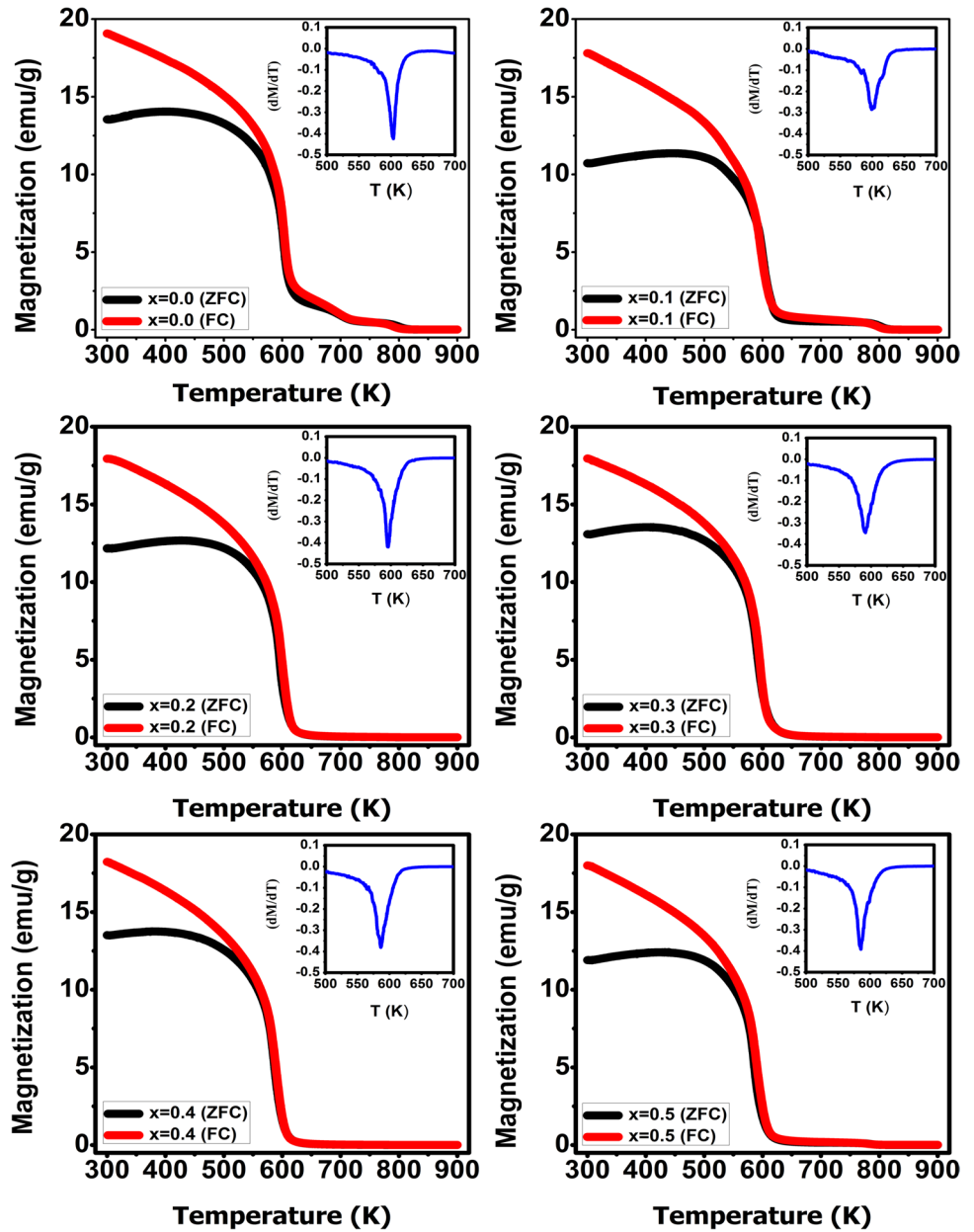


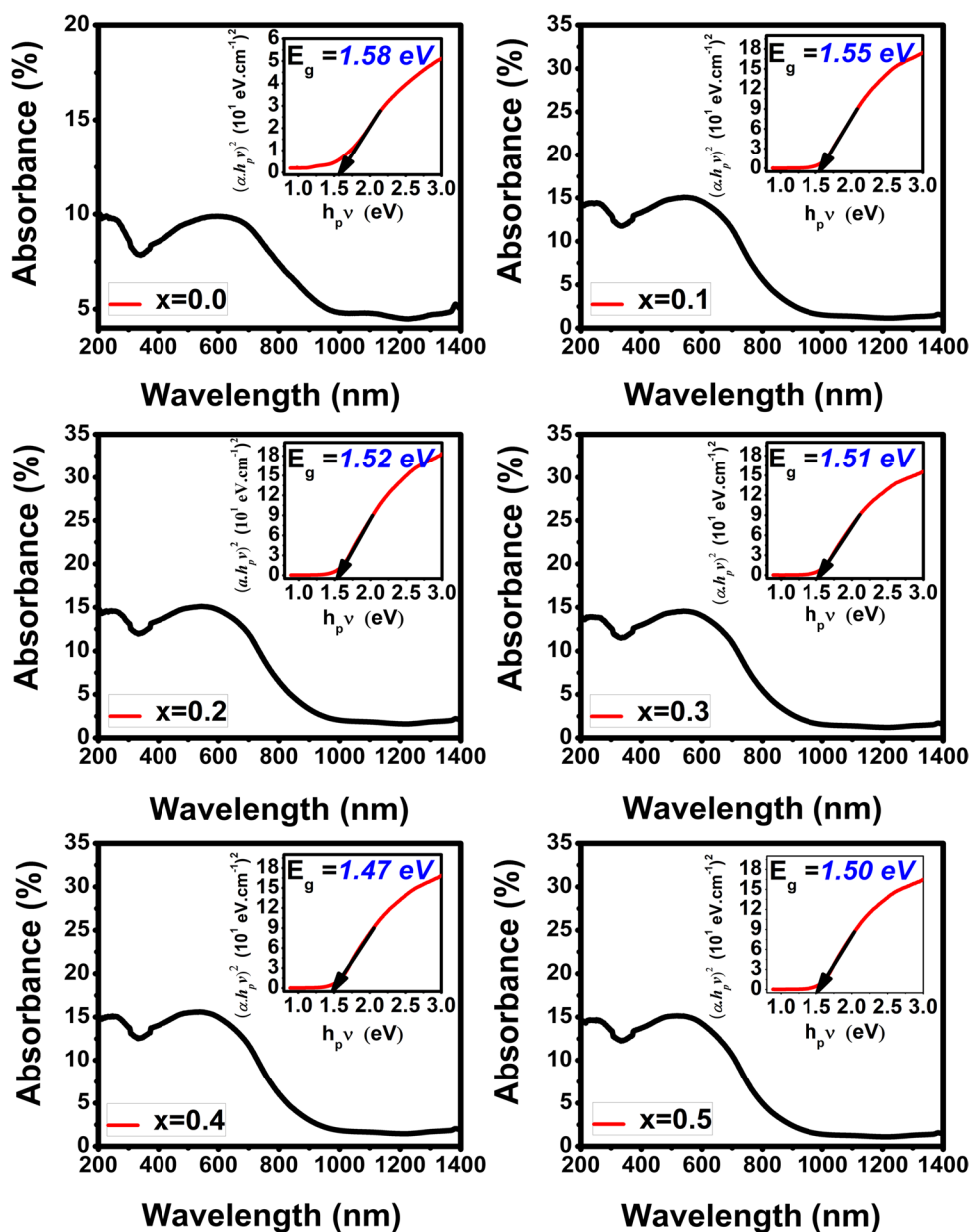
Table 3 Saturation magnetization (M_s), number of Bohr magneton (N_{bm}), coercivity (H_c), magnetic retentivity (M_r), squareness ratio, magnetic anisotropy constant (K_1), and Curie Temperature (T_c) of the calcined $Ba_2Co_2Fe_{12-x}Ti_xO_{22}$ ($x = 0.0, 0.1, 0.2, 0.3, 0.4,$ and 0.5) ferrite powders

Composition	M_s (emu/g)	Bohr magneton	H_c (Oe)	M_r (emu/g)	(M_r/M_s)	$KI(HA^2/Kg)$	Curie Temperature (K)
$x = 0.0$	43.39	10.55	160.84	8.78	0.2023	3.49×10^{-1}	603.76
$x = 0.1$	40.73	9.89	156.05	8.74	0.2145	3.18×10^{-1}	599.09
$x = 0.2$	40.42	9.81	222.24	10.6	0.2622	4.49×10^{-1}	595.84
$x = 0.3$	38.35	9.31	155.48	8.66	0.2258	2.98×10^{-1}	591.19
$x = 0.4$	36.95	8.96	139.25	8.83	0.2389	2.57×10^{-1}	586.52
$x = 0.5$	36.81	8.92	120.66	7.54	0.2048	2.22×10^{-1}	585.71

with the substitution of Ti^{4+} ions. The decreasing order can be explained on behalf of structural defects and enhanced lattice distortions associated with substituting a larger cation into the hexaferrite system (Mohammed et al. 2021). It can also be associated with the increasing lattice parameter, which provides enhanced inter-atomic spacing, so the atoms can vibrate with large amplitude by utilizing thermal energy. This atomic vibration allows for lowering the electronic potential and lowering the energy bandgap (Naseri and Ghasemi 2016). The decreasing behavior of bandgap (E_g) can also be explained by the valency of both ions. Ti^{4+} ions have a higher valency state which substitutes for Fe^{3+} ions having a lower valency state. It generates impurity energy levels (donor type), which are responsible

for the narrow bandgap (Cai et al. 2014). A slight enhancement of the bandgap (observed with $x=0.5$) value can be explained by the dominance of the second factor, i.e., quantum confinement with decreasing particle size. The confinement of both electrons and holes within the nanoscale premises allows for the widening of the bandgap within semiconductors (El-Hagary et al. 2019; Singh and Rajput 2020). Due to enhanced photon absorption, along with the lowest bandgap energy (narrow bandgap results in the easy absorption of photon energy), two samples, $\text{Ba}_2\text{Co}_2\text{Fe}_{12}\text{O}_{22}$ (pristine $\text{Co}_2\text{-Y}$ hexaferrite) and $\text{Ba}_2\text{Co}_2\text{Fe}_{11.6}\text{Ti}_{0.4}\text{O}_{22}$ (titanium substituted $\text{Co}_2\text{-Y}$ hexaferrite), are studied for its comparative photocatalytic efficiency within the degradation of a nonbiodegradable dye, i.e., methyl orange (MO).

Fig. 10 UV–Visible diffuse reflectance spectra along with Tauc plot for determination of direct band gap energy of calcined $\text{Ba}_2\text{Co}_2\text{Fe}_{12-x}\text{Ti}_x\text{O}_{22}$ ($x=0.0, 0.1, 0.2, 0.3, 0.4,$ and 0.5) ferrite powders



Photocatalytic analysis

The photocatalytic efficiency of $\text{Ba}_2\text{Co}_2\text{Fe}_{12}\text{O}_{22}$ and $\text{Ba}_2\text{Co}_2\text{Fe}_{11.6}\text{Ti}_{0.4}\text{O}_{22}$ ferrites are investigated for the degradation of methyl orange in an aqueous solution at room temperature with a pH level of 3. The MO degradation performance on the $\text{Ba}_2\text{Co}_2\text{Fe}_{11.6}\text{Ti}_{0.4}\text{O}_{22}$ photocatalyst was checked under different pH conditions. Optimum MO degradation was observed at pH ~ 3 conditions (Fig. S1). The suitable selectivity of pH value decides the interaction between the catalyst and pollutant. The pH value of 3 is optimized by an earlier published study for the degradation of methyl orange within similar conditions (De et al. 2020). Figure 11 shows negligible MO degradation occurs in an aqueous solution containing H_2O_2 , either in the dark or under visible light irradiation, even after 50 min of test time. Figure 12a depicts the change in MO absorbance (with time) when mixed with $\text{Ba}_2\text{Co}_2\text{Fe}_{12}\text{O}_{22}$ particles in an aqueous suspension with H_2O_2 in the dark. There was virtually no change in MO absorbance even after 90 min under dark conditions.

The photocatalytic reaction mixture is kept in the dark for 15 min to ensure the adsorption–desorption equilibrium on the photocatalyst’s surface. UV–visible data for the dark condition (light off) is incorporated in Fig. S2. Under the light-off condition, the dye gets adsorbed on the photocatalyst’s surface in the first 10 min. Then, the reaction mixture is kept in the dark for another 5 min. During this interval (last 5 min), there is no change in MO concentration (as shown in Fig. S2), confirming the achievement of adsorption–desorption equilibrium of MO on the photocatalyst’s surface. Nevertheless, there is a slight decrease in MO absorbance (in the presence of $\text{Ba}_2\text{Co}_2\text{Fe}_{12}\text{O}_{22}$ particles) under visible light irradiation. The result shows that the MO degradation on $\text{Ba}_2\text{Co}_2\text{Fe}_{12}\text{O}_{22}$ has poor efficiency under visible light irradiation.

The role of Ti^{4+} substitution over the degradation efficiency can be emphasized by analyzing both pristine and Ti^{4+} substituted samples for their dye degradation efficiency

within similar conditions. The results (as shown in Fig. 13) suggest that the $\text{Ba}_2\text{Co}_2\text{Fe}_{11.6}\text{Ti}_{0.4}\text{O}_{22}$ can efficiently degrade (nearly complete) the methyl orange (MO) within the test time of 90 min. The comparative performance of both these catalysts is analyzed based on the degradation rate for methyl orange, as shown in Fig. 14a. It describes the time-dependent variation of MO concentration (C) at the time (t) with respect to the initial concentration (C_o), i.e., 4.6 mg/l. To quantify the performance of both these catalysts and determination of heterogeneously catalyzed kinetics of the MO photodegradation, a standard Langmuir–Hinshelwood (L–H) equation is utilized with the following expression (Almahri 2022).

$$\ln(C/C_o) = -k_{arc}t \quad (14)$$

where t is time in minutes, k_{arc} is the apparent rate constant or pseudo-first-order rate constant. The rate constants (k_{arc}) are determined as the slope of $\ln(C/C_o)$ vs. time plots (shown in Fig. 14b). The rate constant values for $\text{Ba}_2\text{Co}_2\text{Fe}_{12}\text{O}_{22}$ and $\text{Ba}_2\text{Co}_2\text{Fe}_{11.6}\text{Ti}_{0.4}\text{O}_{22}$ are found to be 2.7×10^{-3} and $1.9 \times 10^{-2} \text{ min}^{-1}$, respectively.

The error analysis is carried out for photo-Fenton MO degradation kinetics on $\text{Ba}_2\text{Co}_2\text{Fe}_{12}\text{O}_{22}$ and $\text{Ba}_2\text{Co}_2\text{Fe}_{11.6}\text{Ti}_{0.4}\text{O}_{22}$ nanoparticles. The standard deviation of the collected data points is calculated as the error. Figure 15a displays the error bar diagram, whereas, in a few points, the error bar is not visible because they are minor than the symbol size. Quenching experiments are also carried out in the presence of different radical or active species-trapping agents. A particular quencher can quench a specific reactive species and affect the photocatalytic performance of the catalyst. Isopropyl alcohol (IPA) and parabenzquinone (PBQ) can specifically quench hydroxyl radical ($\cdot\text{OH}$) and superoxide radical ($\text{O}_2^{\cdot-}$), respectively. As shown in Fig. 15b, the addition of IPA and PBQ decreases the photocatalytic activity with respect to without quencher. Hence,

Fig. 11 MO degradation in the absence of heterogeneous catalyst using H_2O_2 under dark conditions (a) and the presence of a visible light source (b)

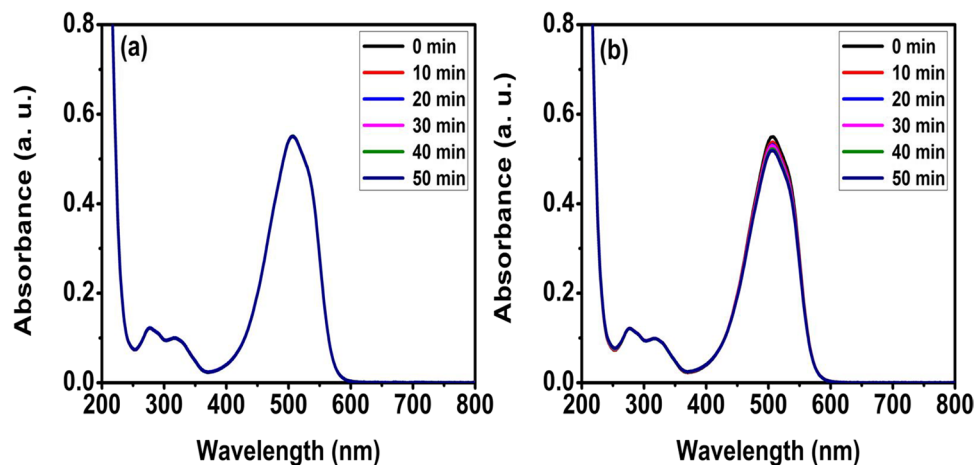


Fig. 12 MO degradation with $\text{Ba}_2\text{Co}_2\text{Fe}_{12}\text{O}_{22}$ as a heterogeneous catalyst in the presence of H_2O_2 within dark conditions (a) and the presence of a visible light source (b)

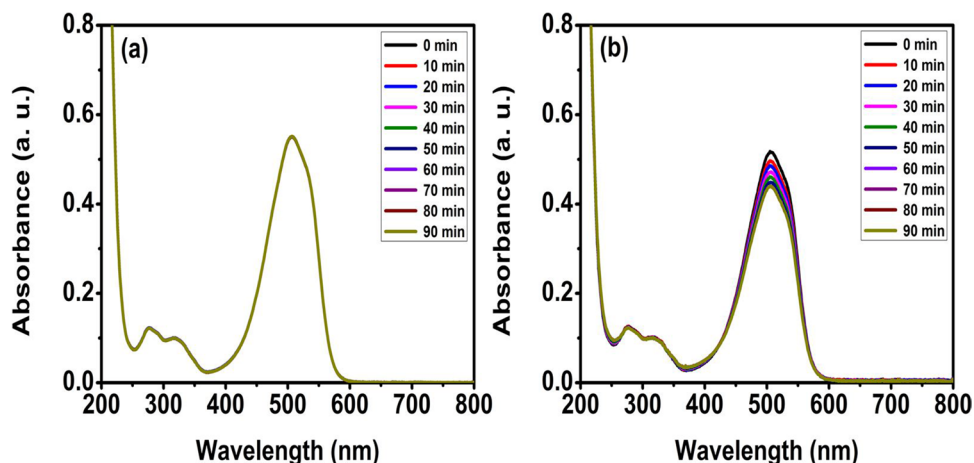


Fig. 13 Photocatalytic MO degradation on $\text{Ba}_2\text{Co}_2\text{Fe}_{11.6}\text{Ti}_{0.4}\text{O}_{22}$ nanoparticles with H_2O_2 under dark reaction condition (a) and visible light irradiation (b)

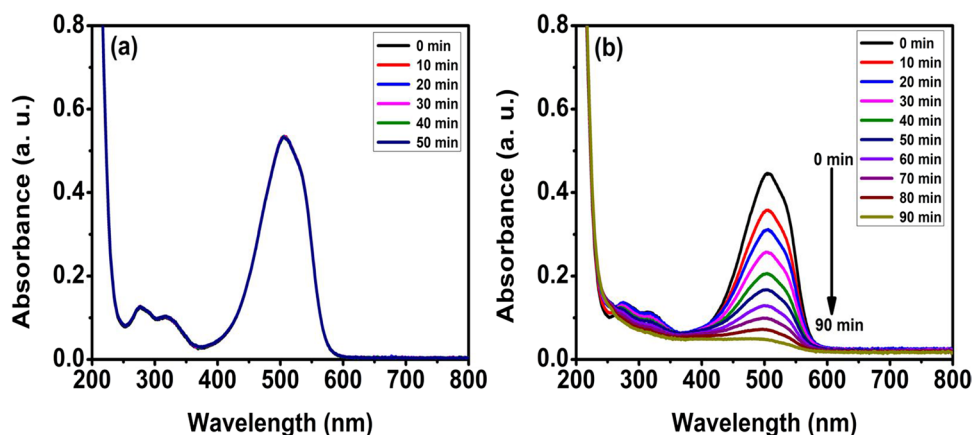
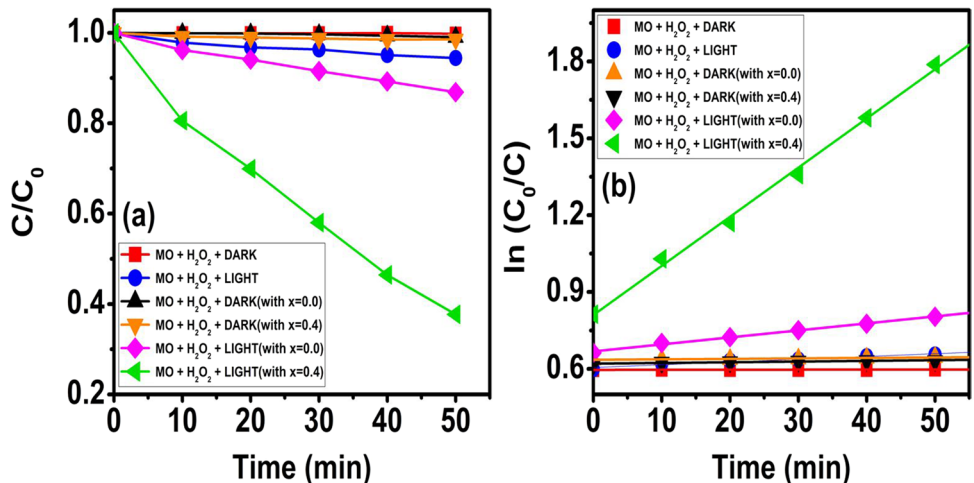


Fig. 14 a Comparative analysis of MO degradation with $\text{Ba}_2\text{Co}_2\text{Fe}_{12}\text{O}_{22}$ and $\text{Ba}_2\text{Co}_2\text{Fe}_{11.6}\text{Ti}_{0.4}\text{O}_{22}$ under various controlled conditions. b Comparison of first-order kinetics ($\ln(C_0/C)$ vs. time plot) of both catalysts



the hydroxyl radical ($\cdot\text{OH}$) and superoxide radical ($\text{O}_2^{\cdot-}$) are prime reactive species for photocatalytic MO degradation.

Another significant parameter, i.e., the turnover frequency (TOF), is also examined in these hexaferrite catalysts to compare the photocatalytic degradation performances within similar conditions. The turnover frequency

is the number of reactants converted into a product on 1 g of heterogeneous catalyst in a unit of time (Shang et al. 2013). The turnover frequency values for $\text{Ba}_2\text{Co}_2\text{Fe}_{12}\text{O}_{22}$ and $\text{Ba}_2\text{Co}_2\text{Fe}_{11.6}\text{Ti}_{0.4}\text{O}_{22}$ are found to be 7.49×10^{-7} and $3.93 \times 10^{-6} \text{ mol g}^{-1} \text{ min}^{-1}$, respectively. In a combined consideration of both the apparent rate constant (k_{arc}) and

turnover frequency (TOF) values, the titanium substituted sample $\text{Ba}_2\text{Co}_2\text{Fe}_{11.6}\text{Ti}_{0.4}\text{O}_{22}$ shows the best performance with complete degradation of the methyl orange dye within 90 min. This enrichment of catalytic activity can be correlated to various factors such as enhanced absorbance value, lowest band gap value, and fine particle size to facilitate the larger reactive sites.

Morphological analysis

The surface morphological features of titanium-substituted $\text{Co}_2\text{-Y}$ hexaferrite ($\text{Ba}_2\text{Co}_2\text{Fe}_{11.6}\text{Ti}_{0.4}\text{O}_{22}$) are analyzed using scanning electron micrographs. Figure 16 displays the micrographs of calcined powder at 5 K and 20 K magnifications along with corresponding EDX spectra, which confirms the elemental identity of this compound without any traces of impurity elements. The surface morphology reveals that the hexaferrite powder has a wide range of size distribution (from 0.15 to 3.61 μm) with an average particle size of 1.435 μm (standard deviation of 0.718), composed of the larger hexagonal plate-like particle along with small particles (irregular shaped) distributed over the surface of these larger particles.

Surface electronic structures analysis

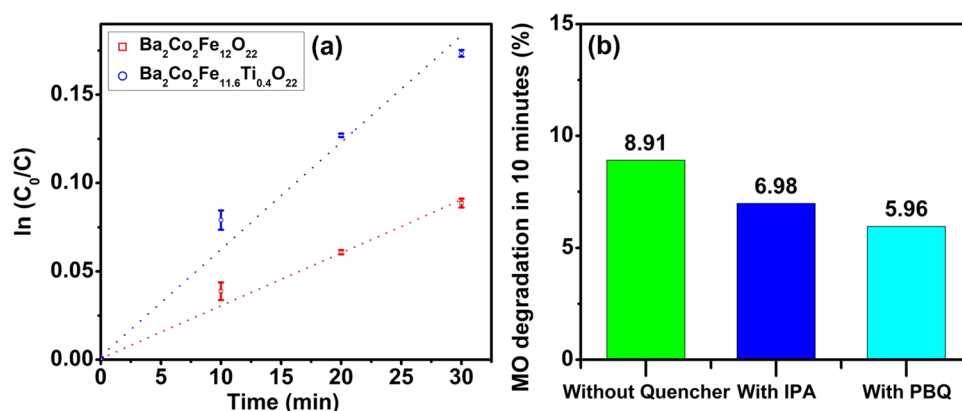
To validate the successful substitution of Ti^{4+} ions within the $\text{Ba}_2\text{Co}_2\text{Fe}_{11.6}\text{Ti}_{0.4}\text{O}_{22}$ hexaferrite sample, the electronic structures of all the elements are studied using XPS spectra recorded in the range of 1350 eV to 1 eV region. The relative contribution of each valance state is demonstrated qualitatively by deconvoluting the high-resolution X-ray photoelectron spectrum.

A wide scan of XPS spectra, displayed in Fig. 17a, validates the existence of Ba, Co, Fe, Ti, and O elements within it, without any impurity element except carbon. The atomic percentage of the compound is quantified using a normalized peak area ratio within the overall XPS spectra (utilizing CasaXPS software). The precise measurement of peak areas

requires the selection of a proper deconvolution method and background removal, which can resolve the peak broadening mechanisms in XPS (Cabrera-German et al. 2016). The atomic percentage obtained within the XPS spectra is shown in Fig. 17a. The atomic percentage at the surface XPS spectra is found to be in good agreement with the concerned chemical formula, measured with EDX spectra, describing good homogeneities within the synthesized sample.

The respective $\text{C}1s$ peak position (considered as an internal standard to calibrate the XPS data) is adjusted to 284.8 eV to compensate for the binding energies associated with all other peaks (Wu et al. 2015; Suthar et al. 2020). The high-resolution $\text{C}1s$ spectra, displayed in Fig. 17b, reveal the existence of three peaks (obtained through deconvolution of spectra) corresponding to the C–C bonding (284.80 eV), C–O–C bond (285.83 eV), O=C–O bond (287.76 eV), correspondingly (Wu et al. 2019). The high-resolution $\text{Ba-}3d$ spectra, displayed in Fig. 17c, confirm the existence of spin–orbit doublet for barium ions (Ba^{2+} state), consistent with $\text{Ba-}3d_{5/2}$ at 779.13 eV and $\text{Ba-}3d_{3/2}$ at 794.45 eV, having an energy interval of 15.32 eV (Suthar et al. 2020). The high-resolution $\text{Co-}2p$ spectra, displayed in Fig. 17d, support the existence of spin–orbit doublet for cobalt ions (Co^{2+} state), consistent with $\text{Co-}2p_{3/2}$ at 779.13 eV and $\text{Co-}2p_{1/2}$ at 794.46 eV having an energy interval of 15.33 eV along with two satellite peaks at 785.06 eV and 803.22 eV, correspondingly (Suthar et al. 2020). The high-resolution $\text{Fe-}2p$ spectra, displayed within Fig. 17e, verify the existence of characteristic peaks for iron ions (mixed Fe^{3+} and Fe^{2+} states), consistent with $\text{Fe-}2p_{3/2}$ at 709.98 eV and $\text{Fe-}2p_{1/2}$ at 723.48 eV having an energy interval of 13.5 eV along with two satellite peaks at 718.20 eV and 732.47 eV, correspondingly. The further deconvolution of these two major characteristic peaks explains the co-existence of mixed valency states of iron ions within each orbit corresponding to $\text{Fe}^{2+}\text{-}2p_{3/2}$ at 709.50 eV, $\text{Fe}^{2+}\text{-}2p_{1/2}$ at 723.18 eV, $\text{Fe}^{3+}\text{-}2p_{3/2}$ at 711.62 eV and $\text{Fe}^{3+}\text{-}2p_{1/2}$ at 725.11 eV (Suthar et al. 2020). The high-resolution $\text{Ti-}2p$ spectra, displayed within Fig. 17f, justify the existence of characteristic peaks for titanium ions (mixed

Fig. 15 **a** Error bar diagram for the comparison of photo-Fenton MO degradation performance by the catalyst, $\text{Ba}_2\text{Co}_2\text{Fe}_{12}\text{O}_{22}$, and $\text{Ba}_2\text{Co}_2\text{Fe}_{11.6}\text{Ti}_{0.4}\text{O}_{22}$. **b** Quenching experiment results on the catalyst, $\text{Ba}_2\text{Co}_2\text{Fe}_{11.6}\text{Ti}_{0.4}\text{O}_{22}$



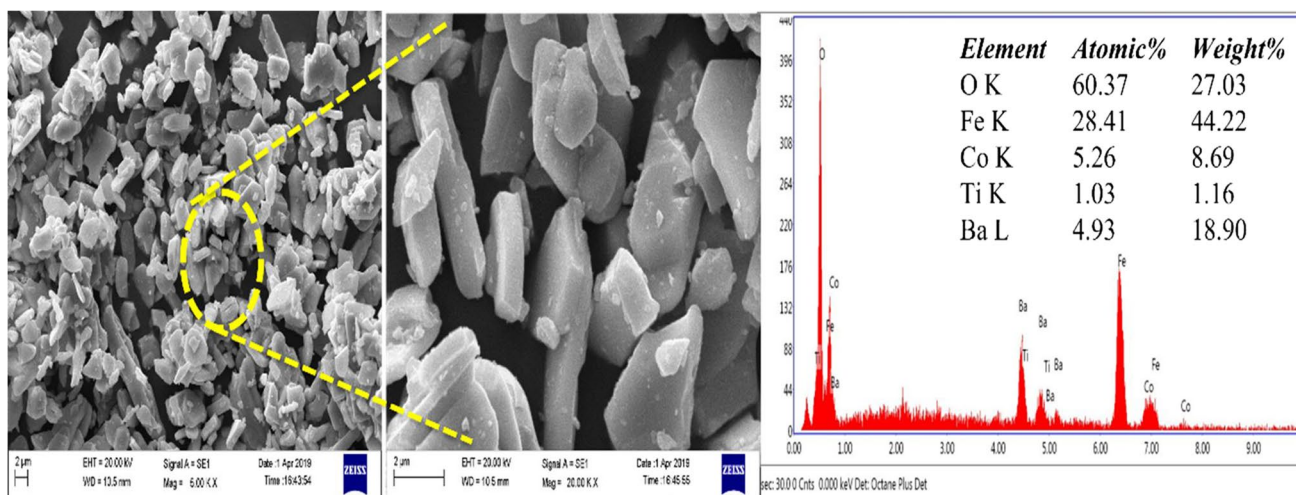


Fig. 16 SEM micrographs of calcined $\text{Ba}_2\text{Co}_2\text{Fe}_{11.6}\text{Ti}_{0.4}\text{O}_{22}$ hexaferrite powder at two different magnifications of 5 K and 20 K, along with EDX analysis

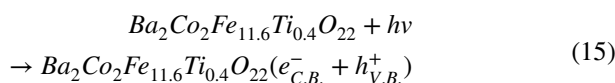
Ti^{3+} and Ti^{4+} states), consistent with $\text{Ti}-2p_{3/2}$ at 457.48 eV and $\text{Ti}-2p_{1/2}$ at 463.28 eV having an energy interval of 5.8 eV. The further deconvolution of these two major characteristic peaks explains the co-existence of mixed valency states of titanium ions within each orbit corresponding to $\text{Ti}^{3+}-2p_{3/2}$ at 457.50 eV, $\text{Ti}^{3+}-2p_{1/2}$ at 463.13 eV, $\text{Ti}^{4+}-2p_{3/2}$ at 458.70 eV, and $\text{Ti}^{4+}-2p_{1/2}$ at 464.92 eV (Woo et al. 2020). The high-resolution $\text{O}1s$ spectra, displayed within Fig. 17g, reveal the existing two peaks (obtained through deconvolution of spectra) corresponding to M–O bonds at 528.98 eV and oxygen vacancy (O^{1-}) at 530.62 eV, correspondingly (Suthar et al. 2020). The XPS study suggests the mixed ionic states for iron ions (Fe^{2+} and Fe^{3+}) and titanium ions (Ti^{3+} and Ti^{4+}) within the sample. It may facilitate electron transportation and enhance redox configuration to the sample $\text{Ba}_2\text{Co}_2\text{Fe}_{11.6}\text{Ti}_{0.4}\text{O}_{22}$ (Woo et al. 2020). The existence of oxygen vacancy also helps to understand the enhanced photocatalytic activity. The presence of oxygen vacancy improves visible light absorption. It leads to narrowing the bandgap of the sample by generating an extra impurity level adjacent to the valence band (Wang et al. 2012; Fernández-Clement et al. 2020).

Plausible pathway for photocatalytic degradation of MO

The $\text{Ba}_2\text{Co}_2\text{Fe}_{11.6}\text{Ti}_{0.4}\text{O}_{22}$ hexaferrite has a narrow bandgap value ($E_g = 1.47$ eV) as compared to the $\text{Ba}_2\text{Co}_2\text{Fe}_{12}\text{O}_{22}$ ($E_g = 1.58$ eV). It shows excellency within the photocatalytic degradation of methyl orange (MO). The degradation process (termed as the Photo-Fenton type process) is performed with H_2O_2 and under visible light irradiation, which degrades the MO from the wastewater by generating

the active hydroxyl radicals (OH^\bullet). It appears that Ti doping of $\text{Ba}_2\text{Co}_2\text{Fe}_{12}\text{O}_{22}$ significantly improves the photocatalytic reductive cleavage of H_2O_2 for enhanced hydroxyl radical generation. These radicals are strong oxidants (2.84 V with respect to a standard hydrogen electrode (SHE)) (Chahar et al. 2021). Ti-doping of $\text{Ba}_2\text{Co}_2\text{Fe}_{12}\text{O}_{22}$ could also improve its interaction with MO molecules in an acidic medium (Kumar et al. 2022). The visible light plays a crucial role in this degradation process by generating photogenerated electron–hole pairs by absorption of photon energy, and the electron moves from the valence band to the conduction band. These electrons (e^-) and holes (h^+) are responsible for conducting redox reactions, resulting in the generation of hydroxyl radicals (OH^\bullet), as shown in Fig. 18a. The generation of hydroxyl radicals (OH^\bullet) can also be understood with the electronic transition during the oxidation and reduction of transition metal cations, as shown in Fig. 18b. The releasing electron with the oxidation of Ti^{3+} and Fe^{2+} is utilized to generate active hydroxyl radicals (OH^\bullet). The generation of these hydroxyl radicals (OH^\bullet) can be explained using the following steps (Sharma et al. 2015):

Step 1. Absorption of photon energy and generation of electron–hole pair



Step 2. Utilization of photogenerated electron ($e_{C.B.}^-$) by H_2O_2

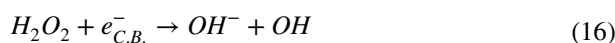
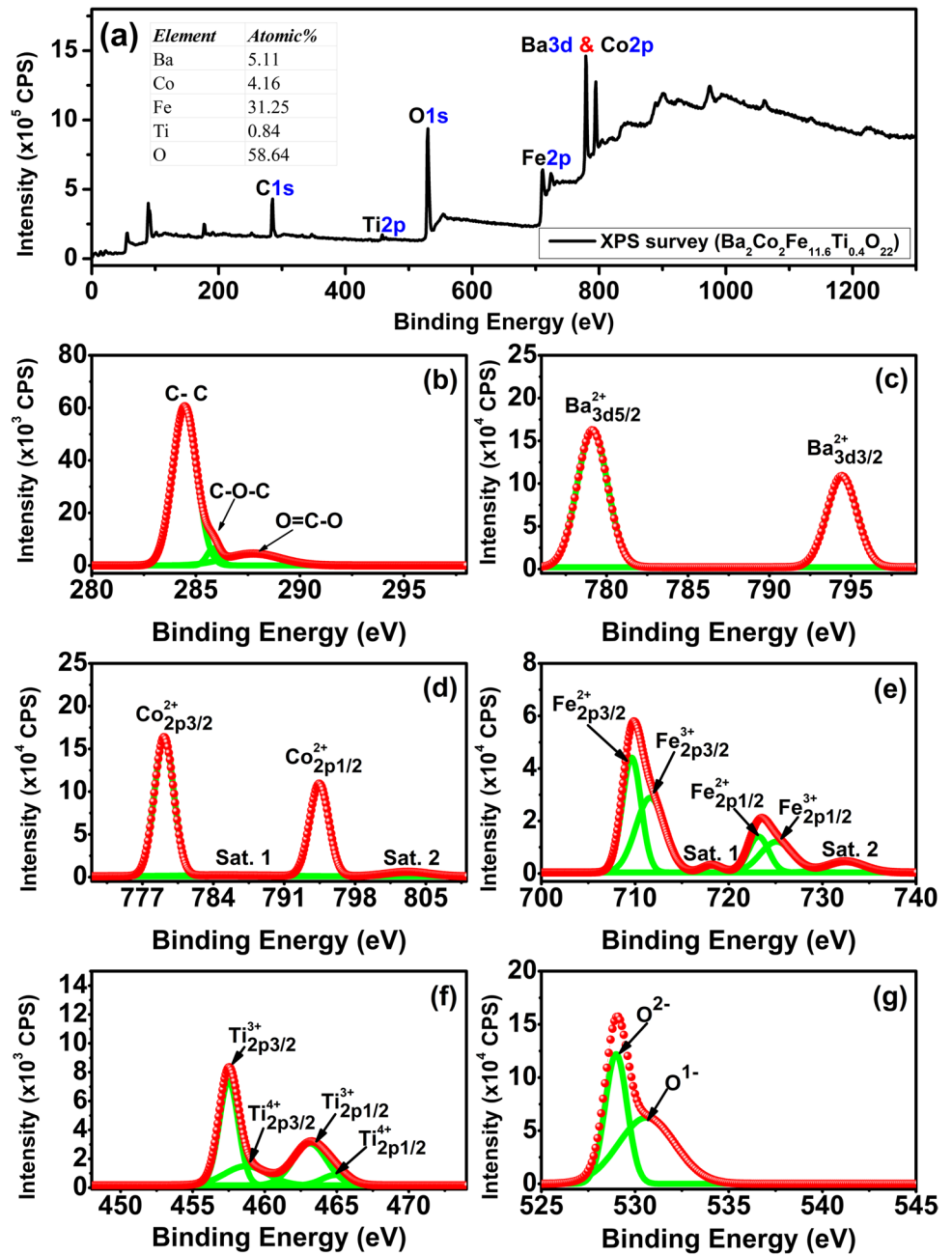


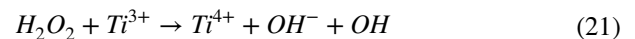
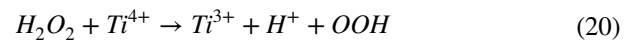
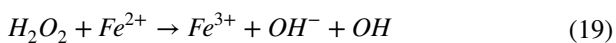
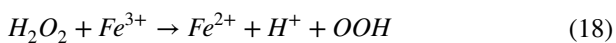
Fig. 17 The XPS analysis of $\text{Ba}_2\text{Co}_2\text{Fe}_{11.6}\text{Ti}_{0.4}\text{O}_{22}$ hexaferri-rite wide scan XPS survey (a) and high-resolution core spectra of C-1s (b), Ba-3d (c), Co-2p (d), Fe-2p (e), Ti-2p (f), and O-1s (g)



Step 3. Utilization of photogenerated hole ($h_{V.B.}^+$) by hydroxyl ion (OH^-)



Step 4. The reaction of H_2O_2 with transition metal cations situated over the catalytic surface.



The hydroxyl radicals generated through these steps within the process degrade the methyl orange dye, as follows.

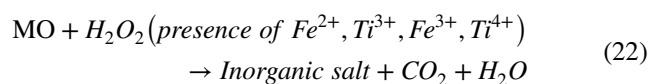
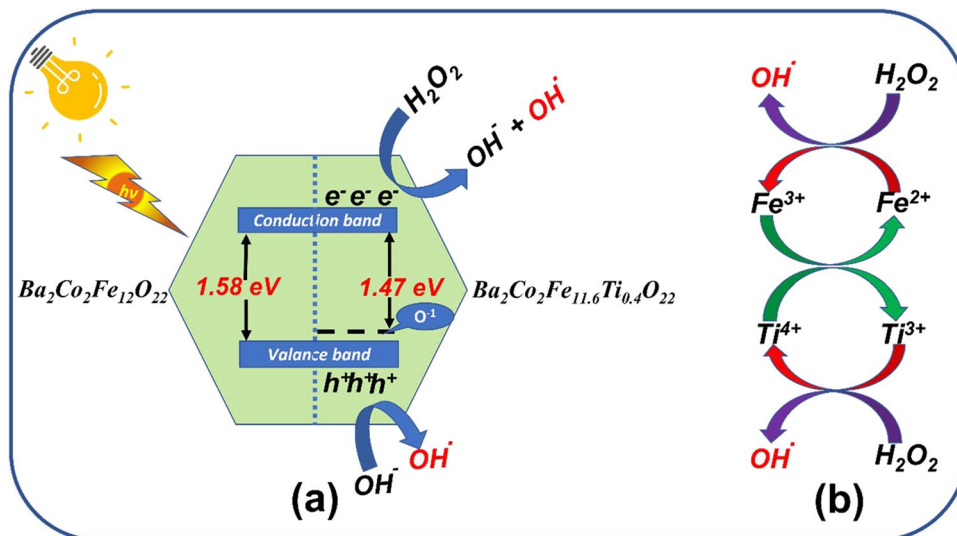


Fig. 18 **a** Plausible mechanism for the generation of hydroxyl radicals (OH^\bullet) within the Photo-Fenton-based $\text{Co}_2\text{-Y}$ type hexaferrite ferrite/ H_2O_2 system, **b** generation of active hydroxyl radicals (OH^\bullet) by relocating electrons within the $\text{Ba}_2\text{Co}_2\text{Fe}_{11.6}\text{Ti}_{0.4}\text{O}_{22}$ hexaferrite system



The superiority of the proposed titanium-substituted $\text{Co}_2\text{-Y}$ hexaferrite can be understood with a comparative analysis (as shown in Table 4) of various catalytic systems studied earlier for photocatalytic degradation of nonbiodegradable pollutants. The analysis suggests that the $\text{Ba}_2\text{Co}_2\text{Fe}_{11.6}\text{Ti}_{0.4}\text{O}_{22}$ hexaferrite possesses a higher apparent rate constant value among all studied systems. It shows a faster degradation response and provides an advantageous step toward developing a

magnetically separable heterogeneous photocatalyst. The overall degradation efficiency of $\text{Ba}_2\text{Co}_2\text{Fe}_{11.6}\text{Ti}_{0.4}\text{O}_{22}$ can be correlated with the facile generation of hydroxyl radicals (OH^\bullet) along with small crystallite size, presence of active Ti^{3+} species (promote the interaction of catalyst with reactants, retard the recombination of electron and hole) and Fe^{3+} and Fe^{2+} (responsible for trapping of electrons and holes, alter the recombination rate) (Khan and Swati 2016).

Table 4 Comparative analysis of the apparent rate constant (k_{arc}) and degradation efficiency with the earlier reported photocatalytic systems for the degradation of various pollutants

S. No	Heterogeneous catalyst	Catalyst dose (mg/ml)	Utilized scavenger	k_{arc} (min^{-1})	Pollutant	Degradation efficiency (%)	Reference
1	Meso- CuFe_2O_4	0.3	H_2O_2	1.70×10^{-2}	Imidacloprid	100	Wang et al. (2014)
2	ZnFe_2O_4	1	H_2O_2	3.00×10^{-5}	Reactive black KN-GR	100	Liu et al. (2011)
3	$\text{SrFe}_{12}\text{O}_{19}$	5	-	3.00×10^{-3}	Toluidine blue	100	Farghali et al. (2008)
4	$\text{SrFe}_{12}\text{O}_{19}/\text{SrFeO}_{2.87}$	5	-	5.00×10^{-3}	Toluidine blue	100	Farghali et al. (2008)
5	Bentonite	0.1	H_2O_2	2.40×10^{-3}	Methylene blue	100	Almahri (2022)
6	Bentonite/ MnFe_2O_4	0.1	H_2O_2	1.30×10^{-3}	Methylene blue	100	Almahri (2022)
7	CuFe_2O_4	0.1	H_2O_2	1.30×10^{-3}	Methylene blue	73.8	Qin et al. (2018)
8	CoFe_2O_4	0.2	-	2.00×10^{-4}	Methyl orange	-	Kim et al (2016)
9	$\text{CoFe}_2\text{O}_4/\text{Polyaniline}$	0.2	-	1.61×10^{-2}	Methyl orange	85	Kim et al (2016)
10	$\text{K}_2\text{Fe}_4\text{O}_7$	0.02	H_2O_2	1.30×10^{-3}	Methylene blue	100	Zhang et al. (2020a, b)
11	$\text{Bi}_{0.9}\text{Gd}_{0.1}\text{FeO}_3$	0.01	-	1.21×10^{-2}	Methyl blue	95.60	Arti et al. (2022)
12	$\text{Bi}_{0.9}\text{Gd}_{0.1}\text{Fe}_{0.95}\text{Mn}_{0.05}\text{O}_3$	0.01	-	1.20×10^{-2}	Methyl blue	96.08	Arti et al. (2022)
13	$\text{Bi}_{0.9}\text{Gd}_{0.1}\text{Fe}_{0.95}\text{Co}_{0.05}\text{O}_3$	0.01	-	1.24×10^{-2}	Methyl blue	94.59	Arti et al. (2022)
14	$\text{Bi}_{0.9}\text{Gd}_{0.1}\text{Fe}_{0.95}\text{Cr}_{0.05}\text{O}_3$	0.01	-	1.23×10^{-2}	Methyl blue	95.35	Arti et al. (2022)
15	BiFeO_3	1	H_2O_2	1.30×10^{-2}	Methyl orange	86	Ruby et al. (2020)
16	BaFe_2O_4	1	-	6.00×10^{-3}	Methyl blue	85	Keerthana et al. (2022)
17	MgFe_2O_4	0.6	-	1.64×10^{-2}	Methyl blue	98.8	Waheed et al. (2022)
18	1.0-Zn/ Fe_2O_4	0.75	-	3.67×10^{-2}	Methyl blue	90.5	Mohan et al. (2021)
19	$\text{Cu}_{0.5}\text{Mg}_{0.5}\text{Fe}_2\text{O}_4\text{-TiO}_2$	1	-	1.39×10^{-2}	Rhodamine B	98.4	Tran et al. (2021)
20	$\text{Ba}_2\text{Co}_2\text{Fe}_{11.6}\text{Ti}_{0.4}\text{O}_{22}$	0.05	H_2O_2	1.90×10^{-2}	Methyl orange	100	This work

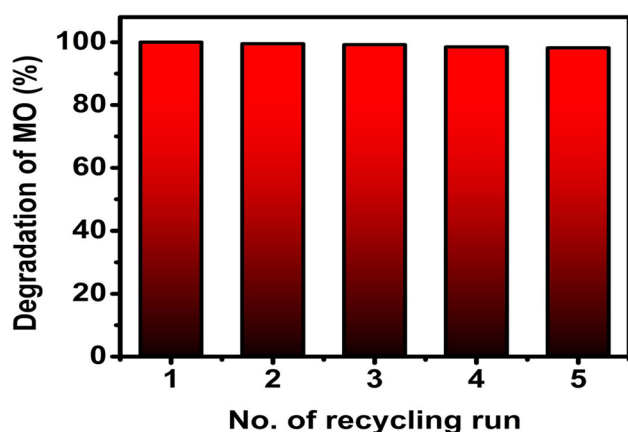


Fig. 19 Reusability of the $\text{Ba}_2\text{Co}_2\text{Fe}_{11.6}\text{Ti}_{0.4}\text{O}_{22}$ hexaferrite as a catalyst for five consecutive recycling runs under similar conditions

Reusability analysis

A better recyclability and chemical stability of any photocatalyst define its suitability for possible adoption in large-scale processes. The re-processibility of the proposed photocatalyst ($\text{Ba}_2\text{Co}_2\text{Fe}_{11.6}\text{Ti}_{0.4}\text{O}_{22}$) was monitored for five consecutive runs after a facile magnetic separation, followed by washing with DI water and drying at 100 °C. The recovered catalyst is again utilized for the same process to degrade the methyl orange from its aqueous solution, keeping all parameters similar to earlier. The results suggest no remarkable degradation efficiency loss (%), as shown in Fig. 19.

Conclusions

The single-phase pristine and Ti^{4+} substituted Y-type barium hexaferrite ($\text{Co}_2\text{-Y}$) having a general formula of $\{\text{Ba}_2\text{Co}_2\text{Fe}_{12-x}\text{Ti}_x\text{O}_{22} (x=0.0, 0.1, 0.2, 0.3, 0.4, \text{ and } 0.5)\}$ are successfully prepared using the nitrate-based sol–gel auto-combustion route. The as-prepared $\text{Co}_2\text{-Y}$ hexaferrite powders have robust thermo-chemical stability, which can overcome the problem associated with spinel-based ferrites. The structural investigations using XRD and FTIR confirm the successful substitution of titanium ions within the hexaferrite system. The magnetic studies confirm the presence of ferrimagnetic nature within all samples. The UV–visible spectrum analysis supports the enhancement in visible light absorption and decreasing behavior for bandgap value by increasing the substitution level of Ti^{4+} ions within the sample. The photocatalytic degradation study of aqueous MO solution in the presence of H_2O_2 suggests the superiority of $\text{Ba}_2\text{Co}_2\text{Fe}_{11.6}\text{Ti}_{0.4}\text{O}_{22}$ compared to pristine $\text{Co}_2\text{-Y}$ barium hexaferrite with an apparent rate constant of $1.9 \times 10^{-2} \text{ min}^{-1}$ and turn over frequency of $3.93 \times 10^{-6} \text{ mol g}^{-1} \text{ min}^{-1}$. This enhanced photocatalytic

activity for sample $\text{Ba}_2\text{Co}_2\text{Fe}_{11.6}\text{Ti}_{0.4}\text{O}_{22}$ can be correlated to the fine crystallite size; the presence of active Ti^{3+} species to promote the reactivity of catalyst surface; the presence of mixed Fe^{3+} and Fe^{2+} to slow down the recombination process by trapping the photogenerated electrons and holes; the existence of oxygen vacancy to enhance the visible light absorption and leads to narrowing the bandgap by creating an extra impurity level adjacent to the valence band. The results suggest that the $\text{Ba}_2\text{Co}_2\text{Fe}_{11.6}\text{Ti}_{0.4}\text{O}_{22}$ ferrite can be utilized as a promising material (facile synthesis, enhanced thermal and chemical stability, and enhanced apparent rate constant value) to catalyze the degradation of several nonbiodegradable organic compounds from wastewater in large-scale industries, without any hazardous footprint on the environment.

Supplementary Information The online version contains supplementary material available at <https://doi.org/10.1007/s11356-023-25432-8>.

Acknowledgements The authors are thankful to the IMPacting Research, INnovation and Technology (IMPRINT) (SERB) (File No: IMP/2019/000165), New Delhi, for the financial support and also grateful to the IIT (BHU) for providing facilities.

Author contribution

- Mukesh Suthar: conceptualization, methodology, validation, formal analysis, investigation, data curation, writing—original draft
- Arup Kumar De: conceptualization, methodology, resources, data curation.
- Arindam Indra: formal analysis, writing—review and editing
- Indrajit Sinha: data curation, writing—review and editing
- Pradip Kumar Roy: resources, supervision, project administration, funding acquisition, writing—review and editing

Data availability On reasonable request, the corresponding author can provide the datasets used and/or analyzed during the current study.

Declarations

Ethical approval Not applicable to this work.

Consent to participate Not applicable.

Consent to publication The final manuscript was reviewed and approved by all authors.

Competing interests The authors declare no competing interests.

References

- Adeela N, Khan U, Iqbal M, Riaz S, Irfan M, Ali H, Javed K, Bukhtiar I, Maaz K, Naseem S (2016) Structural and magnetic response of Mn substituted $\text{Co}_2\text{-Y}$ -type barium hexaferrites. *J Alloy Compd* 686:1017–1024. <https://doi.org/10.1016/j.jallcom.2016.06.239>
- Akhavan O, Azimirad R (2009) Photocatalytic property of Fe_2O_3 nanograin chains coated by TiO_2 nanolayer in visible light irradiation. *Appl Catal A* 369(1–2):77–82. <https://doi.org/10.1016/j.apcata.2009.09.001>

- Al-Jlil SA (2010) Equilibrium study of adsorption of cobalt ions from wastewater using Saudi roasted date pits. *Res J Environ Toxicol* 4(1):1–12. <https://doi.org/10.3923/rjet.2010.1.12>
- Al-Jlil SA (2017) Adsorption of cobalt ions from wastewater on activated Saudi clays. *Appl Water Sci* 7(1):383–391. <https://doi.org/10.1007/s13201-014-0253-z>
- Almahri A (2022) The solid-state synthetic performance of bentonite stacked manganese ferrite nanoparticles: adsorption and photofenton degradation of MB dye and antibacterial applications. *J Market Res* 17:2935–2949. <https://doi.org/10.1016/j.jmrt.2022.02.052>
- Almessiere MA, Slimani Y, Gungunes H, Manikandan A, Baykal A (2019) Investigation of the effects of Tm^{3+} on the structural, microstructural, optical, and magnetic properties of Sr hexaferrites. *Results Physics* 13:102166. <https://doi.org/10.1016/j.rinp.2019.102166>
- Alrebbi TA, Yahaya IK, Mohammed J, Wudil YS, Paray A, Carol TTT, Hafeez HY, Srivastava AK (2022) Phase structure refinement, electric modulus spectroscopy, Urbach energy analysis, and magnetic properties of Ce^{3+} - Ni^{2+} -substituted Y-type barium hexaferrites. *Mater Sci Eng: B* 280:115682. <https://doi.org/10.1016/j.mseb.2022.115682>
- Aroke UO, Momoh RO, Hamidu LAJ, Buhari U (2020) Removal of Azo Dye Methyl Orange in aqueous solution by kaolinite clay: equilibrium isotherms, kinetics and error analyses. *J Eng Technol* 5:422–433. <https://doi.org/10.36348/sjet.2020.v05i11.005>
- Augustin M, Balu T (2017) Estimation of lattice stress and strain in zinc and manganese ferrite nanoparticles by Williamson-Hall and size-strain plot methods. *Int J Nanosci* 16(03):1650035. <https://doi.org/10.1142/S0219581X16500356>
- Auld SM (1907) The relationship between the colour and constitution of organic compounds. *Sci Progress Twentieth Century* (1906-1916) 1(4):650–667. <https://www.jstor.org/stable/43769120>. Accessed 14 Dec 2022
- Baldermann A, Griebbacher AC, Baldermann C, Purgstaller B, Letofsky-Papst I, Kaufhold S, Dietzel M (2018) Removal of barium, cobalt, strontium, and zinc from solution by natural and synthetic allophane adsorbents. *Geosciences* 8(9):309. <https://doi.org/10.3390/geosciences8090309>
- Bilal M, Ihsanullah I, Younas M, Shah MUH (2021) Recent advances in applications of low-cost adsorbents for the removal of heavy metals from water: a critical review. *Separ Purif Technol* 278:119510. <https://doi.org/10.1016/j.seppur.2021.119510>
- Borse PH, Cho CR, Lim KT, Lee YJ, Hong TE, Bae JS, Jeong ED, Kim HJ, Kim HG (2011) Synthesis of barium ferrite for visible light photocatalysis applications. *J Korean Phys Soc* 58(6):1672–1676. <https://doi.org/10.3938/jkps.58.1672>
- Cabrera-German D, Gomez-Sosa G, Herrera-Gomez A (2016) Accurate peak fitting and subsequent quantitative composition analysis of the spectrum of Co 2p obtained with Al K α radiation: I: Cobalt spinel. *Surf Interface Anal* 48(5):252–256. <https://doi.org/10.1002/sia.5933>
- Cai W, Fu C, Gao R, Jiang W, Deng X, Chen G (2014) Photovoltaic enhancement based on improvement of ferroelectric property and band gap in Ti-doped bismuth ferrite thin films. *J Alloy Compd* 617:240–246. <https://doi.org/10.1016/j.jallcom.2014.08.011>
- Carol TTT, Mohammed J, Basandrai D, Godara SK, Bhadu GR, Mishra S, Aggarwal N, Narang SB, Srivastava AK (2020) X-band shielding of electromagnetic interference (EMI) by Co_2Y barium hexaferrite, bismuth copper titanate (BCTO), and polyaniline (PANI) composite. *J Magnet Magnet Mater* 501:166433. <https://doi.org/10.1016/j.jmmm.2020.166433>
- Chahar D, Taneja S, Bisht S, Kesarwani S, Thakur P, Thakur A, Sharma PB (2021) Photocatalytic activity of cobalt substituted zinc ferrite for the degradation of methylene blue dye under visible light irradiation. *J Alloys Comp* 851:156878. <https://doi.org/10.1016/j.jallcom.2020.156878>
- Chai WS, Cheun JY, Kumar PS, Mubashir M, Majeed Z, Banat F, Ho SH, Show PL (2021) A review on conventional and novel materials towards heavy metal adsorption in wastewater treatment application. *J Clean Prod* 296:126589. <https://doi.org/10.1016/j.jclepro.2021.126589>
- Chen L, Chuang Y, Nguyen TB, Chang JH, Lam SS, Chen CW, Dong CD (2020) Novel molybdenum disulfide heterostructure nanohybrids with enhanced visible-light-induced photocatalytic activity towards organic dyes. *J Alloys Comp* 848:156448. <https://doi.org/10.1016/j.jallcom.2020.156448>
- Chen L, Chen CW, Huang CP, Chuang Y, Nguyen TB, Dong CD (2022a) A visible-light sensitive $MoSSe$ nanohybrid for the photocatalytic degradation of tetracycline, oxytetracycline, and chlortetracycline. *J Colloid Interface Sci* 616:67–80. <https://doi.org/10.1016/j.jcis.2022.01.035>
- Chen L, Tsai ML, Chuang Y, Chen CW, Dong CD (2022b) B) Construction of carbon nanotubes bridged MoS_2/ZnO Z-scheme nanohybrid towards enhanced visible light driven photocatalytic water disinfection and antibacterial activity. *Carbon* 196:877–889. <https://doi.org/10.1016/j.carbon.2022.05.055>
- Danaei M, Dehghankhold M, Ataei S, Davarani FH, Javanmard R, Dokhani A, Khorasani S, Mozafari MR (2018) Impact of particle size and polydispersity index on the clinical applications of lipidic nanocarrier systems. *Pharmaceutics* 10(2):57. <https://doi.org/10.3390/pharmaceutics10020057>
- De AK, Majumdar S, Pal S, Kumar S, Sinha I (2020) Zn doping induced band gap widening of Ag_2O nanoparticles. *J Alloys Comp* 832:154127. <https://doi.org/10.1016/j.jallcom.2020.154127>
- Dolia SN, Sharma R, Sharma RP, Saxena NS (2006) Synthesis, X-ray diffraction and optical band gap study of nanoparticles of $NiFe_2O_4$. *Indian J Pure Appl Physics* 44(10):774–776 (<http://nopr.niscares.in/handle/123456789/8367>). Accessed 12 Dec 2022
- Dom R, Subasri R, Radha K, Borse PH (2011) Synthesis of solar active nanocrystalline ferrite, MFe_2O_4 (M: Ca, Zn, Mg) photocatalyst by microwave irradiation. *Solid State Commun* 151(6):470–473. <https://doi.org/10.1016/j.ssc.2010.12.034>
- Benkhaya Said, El Harfi S, Harfi AE (2017) Classifications, properties and applications of textile dyes: a review. *Appl J Environ Eng Sci* 3(3):311–320. <https://doi.org/10.48422/IMIST.PRSM/ajees-v3i3.9681>
- El-Hagary M, Shaaban ER, Moustafa SH, Gad GMA (2019) The particle size-dependent optical band gap and magnetic properties of Fe-doped CeO_2 nanoparticles. *Solid State Sci* 91:15–22. <https://doi.org/10.1016/j.solidstatesciences.2019.03.005>
- ElSayed EE (2018) Natural diatomite as an effective adsorbent for heavy metals in water and wastewater treatment (a batch study). *Water Sci* 32(1):32–43. <https://doi.org/10.1016/j.wsj.2018.02.001>
- Fallmann H, Krutzler T, Bauer R, Malato S, Blanco J (1999) Applicability of the Photo-Fenton method for treating water containing pesticides. *Catal Today* 54(2–3):309–319. [https://doi.org/10.1016/S0920-5861\(99\)00192-3](https://doi.org/10.1016/S0920-5861(99)00192-3)
- Farghali AA, Khedr MH, Moustafa AF (2008) Photocatalytic activity and magnetic properties of nanocrystallite strontium hexaferrite prepared by self-flash combustion. *Mater Technol* 23(2):104–109. <https://doi.org/10.1179/175355508X310089>
- Fattouh F, Rifai L, Habanjar K, Abdallah AM, Hassan RS, Yaacoub N, Awad R (2021) Structural and magnetic properties of hard-soft $BaFe_{12}O_{19}/(Zn_{0.5}Co_{0.5})Fe_2O_4$ ferrites. *J Physics: Condensed Matter* 33(23):235803. <https://doi.org/10.1088/1361-648X/abf478>
- Fernández-Climent R, Giménez S, García-Tecedor M (2020) The role of oxygen vacancies in water splitting photoanodes. *Sustain Energy Fuels* 4(12):5916–5926. <https://doi.org/10.1039/D0SE01305F>

- Fletcher EJ, O'reilly W (1974) Contribution of Fe^{2+} ions to the magnetocrystalline anisotropy constant K_1 of $\text{Fe}_{3-x}\text{Ti}_x\text{O}_4$ ($0 < x < 0.1$). *J Physics C: Solid State Physics* 7(1):171. <https://doi.org/10.1088/0022-3719/7/1/024>
- Arti, Gupta R, Singh SP, Walia R, Kumar V, Verma V (2022) Modification in photovoltaic and photocatalytic properties of bismuth ferrites by tailoring band-gap and ferroelectric properties. *J Alloys Comp* 908:164602. <https://doi.org/10.1016/j.jallcom.2022.164602>
- Hai FI, Yamamoto K, Fukushi K (2007) Hybrid treatment systems for dye wastewater. *Crit Rev Environ Sci Technol* 37(4):315–377. <https://doi.org/10.1080/10643380601174723>
- Holinsworth BS, Mazumdar D, Sims H, Sun QC, Yurtisigi MK, Sarker SK, Gupta A, Butler WH, Musfeldt JL (2013) Chemical tuning of the optical band gap in spinel ferrites: CoFe_2O_4 vs NiFe_2O_4 . *Appl Physics Lett* 103(8):082406. <https://doi.org/10.1063/1.4818315>
- Jacobo S, Regazzoni AE, Blesa MA (2002) Interfacial chemistry of powdered barium ferrites immersed in aqueous solutions: leaching in acidic chloride media. *J Mater Sci* 37(14):3053–3057. <https://doi.org/10.1023/A:1016089502968>
- Jia J, Liu C, Ma N, Han G, Weng W, Du P (2013) Exchange coupling controlled ferrite with dual magnetic resonance and broad frequency bandwidth in microwave absorption. *Sci Technol Adv Mater* 14(4):045002. <https://doi.org/10.1088/1468-6996/14/4/045002>
- Kakol Z, Sabol J, Stickler J, Kozl A, Honig JM (1994) Influence of titanium doping on the magnetocrystalline anisotropy of magnetite. *Phys Rev B* 49(18):12767. <https://doi.org/10.1103/PhysRevB.49.12767>
- Kaveeshwar AR, Kumar PS, Revellame ED, Gang DD, Zappi ME, Subramaniam R (2018) Adsorption properties and mechanism of barium (II) and strontium (II) removal from fracking wastewater using pecan shell based activated carbon. *J Clean Prod* 193:1–13. <https://doi.org/10.1016/j.jclepro.2018.05.041>
- Keerthana SP, Yuvakkumar R, Ravi G, Al-Sehemi AG, Velauthapillai D (2022) Synthesis of pure and lanthanum-doped barium ferrite nanoparticles for efficient removal of toxic pollutants. *J Hazard Mater* 424:127604. <https://doi.org/10.1016/j.jhazmat.2021.127604>
- Kefeni KK, Mamba BB, Msagati TA (2017) Application of spinel ferrite nanoparticles in water and wastewater treatment: a review. *Sep Purif Technol* 188:399–422. <https://doi.org/10.1016/j.seppur.2017.07.015>
- Khan H, Swati IK (2016) Fe^{3+} -doped anatase TiO_2 with d–d transition, oxygen vacancies and Ti^{3+} centers: synthesis, characterization, UV–Vis photocatalytic and mechanistic studies. *Ind Eng Chem Res* 55(23):6619–6633. <https://doi.org/10.1021/acs.iecr.6b01104>
- Kim KN, Jung HR, Lee WJ (2016) Hollow cobalt ferrite–polyaniline nanofibers as magnetically separable visible-light photocatalyst for photodegradation of methyl orange. *J Photochem Photobiol, A* 321:257–265. <https://doi.org/10.1016/j.jphotochem.2016.02.007>
- Kumar P, Kar M (2014) Effect of structural transition on magnetic and optical properties of Ca and Ti co-substituted BiFeO_3 ceramics. *J Alloy Compd* 584:566–572. <https://doi.org/10.1016/j.jallcom.2013.09.107>
- Kumar A, Kumar V, Ghumman SS (2017) Synthesis and characterization of titanium doped barium ferrite and effects of doping on electrical and magnetic properties of the compound. *Ferroelectrics* 519(1):82–89. <https://doi.org/10.1080/00150193.2017.1361215>
- Kumar S, Supriya S, Pandey R, Pradhan LK, Singh RK, Kar M (2018) Effect of lattice strain on structural and magnetic properties of Ca substituted barium hexaferrite. *J Magn Magn Mater* 458:30–38. <https://doi.org/10.1016/j.jmmm.2018.02.093>
- Kumar U, Kuntail J, Kumar A, Prakash R, Pai MR, Sinha I (2022) In-situ H_2O_2 production for tetracycline degradation on $\text{Ag}/\text{s}(\text{Co}_3\text{O}_4/\text{NiFe}_2\text{O}_4)$ visible light magnetically recyclable photocatalyst. *Appl Surf Sci* 589:153013. <https://doi.org/10.1016/j.apsusc.2022.153013>
- Lalegani Z, Nemati A (2015) Effects of Ce–Co substitution on structural, magnetic and dielectric properties of M-type barium hexaferrite nanoparticles synthesized by sol–gel auto-combustion route. *J Mater Sci: Mater Electron* 26(4):2134–2144. <https://doi.org/10.1007/s10854-014-2658-8>
- Lee SG, Kwon SJ (1996) Saturation magnetizations and Curie temperatures of Co–Zn Y-type ferrites. *J Magn Magn Mater* 153(3):279–284. [https://doi.org/10.1016/0304-8853\(95\)00559-5](https://doi.org/10.1016/0304-8853(95)00559-5)
- Lee J, Lee EJ, Hwang TY, Kim J, Choa YH (2020) Anisotropic characteristics and improved magnetic performance of Ca–La–Co-substituted strontium hexaferrite nanomagnets. *Sci Rep* 10(1):1–9. <https://doi.org/10.1038/s41598-020-72608-0>
- Liu L, Zhang G, Wang L, Huang T, Qin L (2011) Highly active S-modified ZnFe_2O_4 heterogeneous catalyst and its photo-Fenton behavior under UV–visible irradiation. *Ind Eng Chem Res* 50(12):7219–7227. <https://doi.org/10.1021/ie2005516>
- Meidanchi A, Akhavan O (2014) Superparamagnetic zinc ferrite spinel–graphene nanostructures for fast wastewater purification. *Carbon* 69:230–238. <https://doi.org/10.1016/j.carbon.2013.12.019>
- Mittal A, Malviya A, Kaur D, Mittal J, Kurup L (2007) Studies on the adsorption kinetics and isotherms for the removal and recovery of Methyl Orange from wastewater using waste materials. *J Hazard Mater* 148(1–2):229–240. <https://doi.org/10.1016/j.jhazmat.2007.02.028>
- Mohammed J, Batoo KM, Abdulaziz AS, Safana AS, Hafeez HY, Raslan EH, Hadi M, Assiafan AAK, Imran A, Srivastava AK (2021) Crystal structure refinement and the magnetic and electro-optical properties of Er^{3+} – Mn^{2+} -substituted Y-type barium hexaferrites. *Ceram Int* 47(13):18455–18465. <https://doi.org/10.1016/j.ceramint.2021.03.169>
- Mohammed J, Batoo KM, Mukhtar G, Labis JP, Raslan EH, Hadi M, Srivastava AK (2022) Crystal-structure analysis, Raman spectroscopy, dielectric measurements, magnetic and optical properties of Cr^{3+} – Ni^{2+} -substituted Co_2Y -type barium hexaferrites. *Mater Res Bull* 145:111564. <https://doi.org/10.1016/j.materresbull.2021.111564>
- Mohan H, Ramalingam V, Adithan A, Natesan K, Seralathan KK, Shin T (2021) Highly efficient visible light driven photocatalytic activity of zinc/ferrite: carbamazepine degradation, mechanism and toxicity assessment. *J Hazard Mater* 416:126209. <https://doi.org/10.1016/j.jhazmat.2021.126209>
- Moradnia F, Fardood ST, Ramazani A, Gupta VK (2020) Green synthesis of recyclable MgFeCrO_4 spinel nanoparticles for rapid photodegradation of direct black 122 dye. *J Photochem Photobiol A: Chem* 392:112433. <https://doi.org/10.1016/j.jphotochem.2020.112433>
- MuhdJulkapli N, Bagheri S, Hamid SBA (2014) Recent advances in heterogeneous photocatalytic decolorization of synthetic dyes. *Sci World J* 2014:692307. <https://doi.org/10.1155/2014/692307>
- Naseri M, Ghasemi R (2016) Structure and physical properties of $\text{Fe}_6\text{O}_8/\text{ba Fe}_6\text{O}_{11}$ nanostructure. *J Magn Magn Mater* 406:200–206. <https://doi.org/10.1016/j.jmmm.2016.01.019>
- National Centre for Biotechnology Information (2022) PubChem Compound Summary for CID 23673835, Methyl orange. [cited 2023 Jan 21. Availabl from <https://pubchem.ncbi.nlm.nih.gov/compound/Methyl-orange>
- Nejad EH, Farzin YA, Heydari MA (2017) Enhancement of soft magnetic properties of La–Zn co-doped nanocrystalline Ni_2Y hexaferrite. *J Magn Magn Mater* 423:226–231. <https://doi.org/10.1016/j.jmmm.2016.09.097>
- Nguyen TD, Phan NH, Do MH, Ngo KT (2011) Magnetic Fe_2MO_4 (M: Fe, Mn) activated carbons: fabrication, characterization and heterogeneous Fenton oxidation of methyl orange. *J Hazard Mater* 185(2–3):653–661. <https://doi.org/10.1016/j.jhazmat.2010.09.068>

- Ounnunkad S (2006) Improving magnetic properties of barium hexaferrites by La or Pr substitution. *Solid State Commun* 138(9):472–475. <https://doi.org/10.1016/j.ssc.2006.03.020>
- Park J, Hong YK, Lee W, An SY, Seo JW, Hur KH (2015) Coercivity of $\text{SrFe}_{12}\text{O}_{19}$ hexaferrite platelets near single domain size. *IEEE Magn Lett* 6:1–3. <https://doi.org/10.1109/LMAG.2015.2460215>
- Pullar RC (2012) Hexagonal ferrites: a review of the synthesis, properties and applications of hexaferrite ceramics. *Prog Mater Sci* 57(7):1191–1334. <https://doi.org/10.1016/j.pmatsci.2012.04.001>
- Qasem NA, Mohammed RH, Lawal DU (2021) Removal of heavy metal ions from wastewater: A comprehensive and critical review. *Npj Clean Water* 4(1):1–15. <https://doi.org/10.1038/s41545-021-00127-0>
- Qin Q, Liu Y, Li X, Sun T, Xu Y (2018) Enhanced heterogeneous Fenton-like degradation of methylene blue by reduced CuFe_2O_4 . *RSC Adv* 8(2):1071–1077. <https://doi.org/10.1039/C7RA12488K>
- Rajivgandhi GN, Ramachandran G, Kanisha CC, Alharbi NS, Kadai-kunnan S, Khaled JM, Alanzi KF, Li WJ (2021) Effect of Ti and Cu doping on the structural, optical, morphological and anti-bacterial properties of nickel ferrite nanoparticles. *Results Physics* 23:104065. <https://doi.org/10.1016/j.rinp.2021.104065>
- Rao KS, Kumar AM, Varma MC, Choudary GSVRK, Rao KH (2009) Cation distribution of titanium substituted cobalt ferrites. *J Alloy Compd* 488(1):L6–L9. <https://doi.org/10.1016/j.jallcom.2009.08.086>
- Rathi BS, Kumar PS (2021) Application of adsorption process for effective removal of emerging contaminants from water and wastewater. *Environ Pollut* 280:116995
- Reddy DHK, Yun YS (2016) Spinel ferrite magnetic adsorbents: alternative future materials for water purification? *Coord Chem Rev* 315:90–111. <https://doi.org/10.1016/j.ccr.2016.01.012>
- Ruby S, Rosaline DR, Inbanathan SSR, Anand K, Kavitha G, Srinivasan R, Umar A, Hegazy HH, Algarni H (2020) Sunlight-driven photocatalytic degradation of methyl orange based on bismuth ferrite (BiFeO_3) heterostructures composed of interconnected nanosheets. *J Nanosci Nanotechnol* 20(3):1851–1858. <https://doi.org/10.1166/jnn.2020.17174>
- Shah P, Unnarkat A, Patel F, Shah M, Shah P (2022) A comprehensive review on spinel-based novel catalysts for visible light assisted dye degradation. *Process Saf Environ Prot* 161:703–722. <https://doi.org/10.1016/j.psep.2022.03.030>
- Shang X, Li B, Zhang T, Li C, Wang X (2013) Photocatalytic degradation of methyl orange with commercial organic pigment sensitized TiO_2 . *Proc Environ Sci* 18:478–485. <https://doi.org/10.1016/j.proenv.2013.04.064>
- Sharma R, Bansal S, Singhal S (2015) Tailoring the photo-Fenton activity of spinel ferrites (MFe_2O_4) by incorporating different cations (M= Cu, Zn, Ni and Co) in the structure. *RSC Adv* 5(8):6006–6018. <https://doi.org/10.1039/C4RA13692F>
- Singh H, Rajput JK (2020) Effect of calcination temperature on magnetic, structural, thermal and optical properties of BFO-T nanoparticles. *SN Appl Sci* 2(8):1–11. <https://doi.org/10.1007/s42452-020-3140-2>
- Singh AK, Hollmann D, Schwarze M, Panda C, Singh B, Menezes PW, Indra A (2021) Exploring the mechanism of peroxodisulfate activation with silver metavanadate to generate abundant reactive oxygen species. *Adv Sustain Syst* 5(4):2000288. <https://doi.org/10.1002/adsu.202000288>
- Suthar M, Srivastava AK, Joshi RK, Roy PK (2020) Nanocrystalline cerium-doped Y-type barium hexaferrite; a useful catalyst for selective oxidation of styrene. *J Mater Sci: Mater Electron* 31(19):16793–16805. <https://doi.org/10.1007/s10854-020-04234-5>
- Tran CV, La DD, Hoai PNT, Ninh HD, Hong PNT, Vu THT, Nadda AK, Nguyen XC, Nguyen DD, Ngo HH (2021) New TiO_2 -doped Cu–Mg spinel-ferrite-based photocatalyst for degrading highly toxic rhodamine B dye in wastewater. *J Hazard Mater* 420:126636. <https://doi.org/10.1016/j.jhazmat.2021.126636>
- Valero-Luna C, Palomares-Sánchez SA, Ruíz F (2016) Catalytic activity of the barium hexaferrite with H_2O_2 /visible light irradiation for degradation of Methylene Blue. *Catal Today* 266:110–119. <https://doi.org/10.1016/j.cattod.2015.08.049>
- Waheed IF, Al-Janabi OYT, Foot PJS (2022) Novel MgFe_2O_4 -CuO/GO heterojunction magnetic nanocomposite: synthesis, characterization, and batch photocatalytic degradation of methylene blue dye. *J Mol Liquids* 357:119084. <https://doi.org/10.1016/j.molliq.2022.119084>
- Wang J, Wang Z, Huang B, Ma Y, Liu Y, Qin X, Zhang X, Dai Y (2012) Oxygen vacancy induced band-gap narrowing and enhanced visible light photocatalytic activity of ZnO . *ACS Appl Mater Interfaces* 4(8):4024–4030. <https://doi.org/10.1021/am300835p>
- Wang Y, Zhao H, Li M, Fan J, Zhao G (2014) Magnetic ordered mesoporous copper ferrite as a heterogeneous Fenton catalyst for the degradation of imidacloprid. *Appl Catal B* 147:534–545. <https://doi.org/10.1016/j.apcatb.2013.09.017>
- Woo SH, Park DS, Choi WS, Kang H, Baek SW, Kim HS, Shin TH, Park JY, Schlegel H, Kim JH (2020) X-ray photoelectron spectroscopic study of impregnated $\text{La}_{0.4}\text{Sr}_{0.6}\text{Ti}_{0.8}\text{Mn}_{0.2}\text{O}_{3+\delta}$ anode material for high temperature-operating solid oxide fuel cell. *Solid State Ionics* 345:115175. <https://doi.org/10.1016/j.ssi.2019.115175>
- Wu LQ, Li YC, Li SQ, Li ZZ, Tang GD, Qi WH, Xue LC, Ge XS, Ding LL (2015) Method for estimating ionicities of oxides using O1s photoelectron spectra. *AIP Adv* 5(9):097210. <https://doi.org/10.1063/1.4931996>
- Wu Y, Lin Y, Xu J (2019) Synthesis of Ag–Ho, Ag–Sm, Ag–Zn, Ag–Cu, Ag–Cs, Ag–Zr, Ag–Er, Ag–Y and Ag–Co metal organic nanoparticles for UV-Vis-NIR wide-range bio-tissue imaging. *Photochem Photobiol Sci* 18(5):1081–1091. <https://doi.org/10.1039/C8PP00493E>
- Yan H, Wang X, Yao M, Yao X (2013) Band structure design of semiconductors for enhanced photocatalytic activity: the case of TiO_2 . *Progress Nat Sci: Mater Int* 23(4):402–407. <https://doi.org/10.1016/j.pnsc.2013.06.002>
- Yang S, Jin R, He Z, Qiao Y, Shi S, Kong W, Wang Y, Liu X (2017) An experimental study on the degradation of methyl orange by combining hydrodynamic cavitation and chlorine dioxide treatments. *Chem Eng Trans* 59:289–294. <https://doi.org/10.33031/CET1759049>
- Youssef NA, Shaban SA, Ibrahim FA, Mahmoud AS (2016) Degradation of methyl orange using Fenton catalytic reaction. *Egypt J Pet* 25(3):317–321. <https://doi.org/10.1016/j.ejpe.2015.07.017>
- Zhang X, Yue Z, Meng S, Yuan L (2014) Magnetic properties of in-plane oriented barium hexaferrite thin films prepared by direct current magnetron sputtering. *J Appl Physics* 116(24):243909. <https://doi.org/10.1063/1.4905028>
- Zhang T, Liu J, Zhou F, Zhou S, Wu J, Chen D, Xu Q, Lu J (2020a) Polymer-coated Fe_2O_3 nanoparticles for photocatalytic degradation of organic materials and antibiotics in water. *ACS Applied Nano Materials* 3(9):9200–9208. <https://doi.org/10.1021/acsanm.0c01829>
- Zhang X, Geng Z, Jian J, He Y, Lv Z, Liu X, Yuan H (2020b) Potassium ferrite as heterogeneous photo-fenton catalyst for highly efficient dye degradation. *Catalysts* 10(3):293. <https://doi.org/10.3390/catal10030293>

Publisher's note Springer Nature remains neutral with regard to jurisdictional claims in published maps and institutional affiliations.

Springer Nature or its licensor (e.g. a society or other partner) holds exclusive rights to this article under a publishing agreement with the author(s) or other rightsholder(s); author self-archiving of the accepted manuscript version of this article is solely governed by the terms of such publishing agreement and applicable law.

Authors and Affiliations

Mukesh Suthar¹ · Arup Kumar De² · Arindam Indra² · Indrajit Sinha² · Pradip Kumar Roy¹ 

✉ Pradip Kumar Roy
pkroy.cer@iitbhu.ac.in

² Department of Chemistry, IIT (BHU), Varanasi 221005, UP,
India

¹ Department of Ceramic Engineering, IIT (BHU),
Varanasi 221005, UP, India